

N-Containing Carbon-Coated β -Si₃N₄ Enhances Si Anodes for High-Performance Li-Ion Batteries

Rahmandhika Firdauzha Hary Hernandha, Bharath Umesh, Purna Chandra Rath, Le Thi Thu Trang, Ju-Chao Wei, Yu-Chun Chuang, Ju Li, and Jeng-Kuei Chang*

The lithiation/delithiation properties of α -Si₃N₄ and β -Si₃N₄ are compared and the carbon coating effects are examined. Then, β -Si₃N₄ at various fractions is used as the secondary phase in a Si anode to modify the electrode properties. The incorporated β -Si₃N₄ decreases the crystal size of Si and introduces a new N–Si–O species at the β -Si₃N₄/Si interface. The nitrogen from the milled β -Si₃N₄ diffuses into the surface carbon coating during the carbonization heat treatment, forming pyrrolic nitrogen and C–N–O species. The synergistic effects of combining β -Si₃N₄ and Si phases on the specific capacity are confirmed. The operando X-ray diffraction and X-ray photoelectron spectroscopy data indicate that β -Si₃N₄ is partially consumed during lithiation to form a favorable Li₃N species at the electrode. However, the crystalline structure of the hexagonal β -Si₃N₄ is preserved after prolonged cycling, which prevents electrode agglomeration and performance deterioration. The carbon-coated β -Si₃N₄/Si composite anode shows specific capacities of 1068 and 480 mAh g⁻¹ at 0.2 and 5 A g⁻¹, respectively. A full cell consisting of the carbon-coated β -Si₃N₄/Si anode and a LiNi_{0.8}Co_{0.1}Mn_{0.1}O₂ cathode is constructed and its properties are evaluated. The potential of the proposed composite anodes for Li-ion battery applications is demonstrated.

Graphitized carbon is commonly used as a negative electrode in commercial LIBs. However, its limited capacity (theoretically, 372 mAh g⁻¹) does not meet the escalating application requirements. Improvement that can lead to better electrode capacity is thus urgently needed. As an alternative, Si-based anodes are highly promising for meeting the required properties.^[3,4] Si is an abundant material (28% of the Earth's crust by mass) with a high theoretical capacity of ≈ 3579 mAh g⁻¹, desirable redox potential, low cost, and non-toxicity.^[5-7] Despite these appealing features, Si anodes suffer from large volume variation (>300%) during cycling, which leads to electrode mechanical degradation and an unstable solid-electrolyte interphase (SEI). Various strategies have been developed to fabricate diverse nano-architectures, such as carbon-coated,^[8] core-shell/yolk-shell,^[9] hollow,^[10] porous,^[11] fibrous,^[12] tubular,^[13] and micropillar^[14] Si-based composites, for improving cycling stability. However, the long-term cyclability of Si-based anodes is not yet satisfactory.^[15] A more robust and reliable Si electrode with a high capacity, superior rate capability, and reasonable cycle life is desirable.

Introducing a secondary phase to alleviate the Si volume change during charge–discharge cycling has been proven to be an effective strategy for reducing stress localization

1. Introduction

Advancements in Li-ion battery (LIB) technology are driven by the rising demand for portable electronic devices, electric vehicles, and large-scale energy storage, especially for renewable sources. Higher energy density is the main target for LIBs.^[1,2]

R. F. H. Hernandha, B. Umesh, P. C. Rath, J.-K. Chang
Department of Materials Science and Engineering
National Yang Ming Chiao Tung University
1001 University Road, Hsinchu 30010, Taiwan
E-mail: jkchang@nycu.edu.tw


L. T. T. Trang, J.-K. Chang
Institute of Materials Science and Engineering
National Central University
300 Zhong-Da Road, Taoyuan 32001, Taiwan

J.-C. Wei
Materials Science Group, National Synchrotron Radiation Research Center
Super Energy Materials Inc.
99-1 Xiyuan Road, Taoyuan 32057, Taiwan

Y.-C. Chuang
National Synchrotron Radiation Research Center
Hsin-Ann Road, Hsinchu 30076, Taiwan

J. Li
Department of Nuclear Science and Engineering and Department of Materials Science and Engineering
Massachusetts Institute of Technology
77 Massachusetts Avenue, Cambridge, MA 02139, USA

J.-K. Chang
Department of Chemical Engineering
Chung Yuan Christian University
200 Chung Pei Road, Taoyuan 32023, Taiwan

 The ORCID identification number(s) for the author(s) of this article can be found under <https://doi.org/10.1002/adv.202301218>

© 2023 The Authors. Advanced Science published by Wiley-VCH GmbH. This is an open access article under the terms of the Creative Commons Attribution License, which permits use, distribution and reproduction in any medium, provided the original work is properly cited.

DOI: 10.1002/adv.202301218

and thus increasing electrode cycling stability.^[16] Accordingly, Si–Cu,^[17] Si–Fe,^[18] Si–Ni,^[19] Si–Ti,^[20] Si–Fe–Cu,^[21] Si–Fe–Ti,^[22] and Si–Ni–Ti^[23] composite anodes have been developed. However, some secondary phases vigorously participate in the lithiation/delithiation reactions and thus undergo substantial volume expansion/contraction,^[18,20,21,23] leading to structural deterioration upon cycling. Furthermore, the introduced silicide phases usually have low Li⁺ conductivity,^[23,24] which results in limited redox kinetics. In addition, the reduced transition metals in the electrodes after lithiation could catalyze electrolyte decomposition^[25–27] and/or change the SEI chemistry and nanostructure.^[28] This may impede Li⁺ transport and ultimately degrade electrode performance. Therefore, the development of a better secondary phase that is mechanically and dimensionally stable and can help the formation of a suitable SEI and effective Li⁺ transport pathways in the Si electrode is important.

A few studies have attempted to incorporate crystalline silicon nitride (Si₃N₄) into Si-based anodes.^[29–32] Crystalline Si₃N₄ has excellent strength and toughness,^[33,34] which are beneficial for mechanically stabilizing Si electrodes. These studies indicated that crystalline Si₃N₄ is inactive in the electrodes.^[29–32] In other words, it neither participated in the lithiation/delithiation reactions nor contributed to the measured capacity. Instead, the Si₃N₄ served as a framework to prevent the Si electrodes from mechanical collapse. Zhang et al. synthesized a composite that consisted of Si particles and α -Si₃N₄ whiskers and found that the inactive α -Si₃N₄ can be a buffer matrix that supports active Si particles and prevents them from aggregating.^[29] Kim et al. prepared a 3D flexible Si composite anode that consisted of core (Si)-shell (α -Si₃N₄) particles and carbon nanofibers.^[30] The Si₃N₄ shells effectively maintained the structural stability of the electrode. Xiao et al. fabricated an egg-like Si/ α -Si₃N₄/C composite anode and reported that a strong and tough α -Si₃N₄ eggshell layer can restrain the structural collapse and facilitate the Li⁺ transport within the electrode.^[31] Of note, crystalline Si₃N₄ exists in two allotropes, namely α -Si₃N₄ and β -Si₃N₄, which exhibit distinct physicochemical properties.^[35] Specifically, β -Si₃N₄ has a higher bulk density than that of α -Si₃N₄.^[36] In addition, β -Si₃N₄ is chemically and thermally more stable than α -Si₃N₄.^[37] α -Si₃N₄ has a trigonal structure, where each nitrogen atom is bonded to three silicon atoms in a distorted trigonal configuration and each silicon atom is tetrahedrally bonded to four nitrogen atoms. In contrast, β -Si₃N₄ has a phenacite structure that consists of a trigonal arrangement of silicon atoms bonded to nitrogen atoms. When viewed along the *c*-axis looking down onto the basal plane of β -Si₃N₄, a hexagonal arrangement of void channels is visible.^[38] The unique crystal structure of β -Si₃N₄ could favor Li⁺ transport and lead to superior electrochemical properties. However, to the best of our knowledge, there have been no studies on the application of β -Si₃N₄ to LIBs, a topic that is worth studying. The fraction and distribution of crystalline Si₃N₄ are considered to crucially impact Si anode performance. The synergistic effects between Si₃N₄ and Si phases have not yet been explored; they need to be examined in detail to further understand the underlying mechanism. It is worth mentioning that a facile, energy-efficient, and scalable synthesis route is desirable for practical LIB applications. A previously reported 3D Si core/ α -Si₃N₄ shell/carbon nanofiber sample was fabricated using electrospinning combined with calcination at 1200 °C.^[30] The egg-like Si/ α -Si₃N₄/C composite was

produced via a two-step reaction, including a nitrification process at 1275 °C and a chemical-vapor-deposition carbon-coating process at 850 °C.^[31] A more convenient and cost-effective method for constructing the desired Si/Si₃N₄ composite is our target.

In this study, the lithiation/delithiation properties of α -Si₃N₄ and β -Si₃N₄ are systematically compared. A carbon coating is deposited on both kinds of particles to enhance electrochemical performance. Then, β -Si₃N₄ and Si at various phase fractions are integrated and their synergistic effects on electrode capacity and rate capability are investigated. The microstructure, crystallinity, chemical composition, and SEI chemistry of various β -Si₃N₄/Si electrodes are studied to explain the synergy. We confirm that the β -Si₃N₄ is not inactive. Operando X-ray diffraction (XRD) is performed to examine the role of β -Si₃N₄ in altering the electrode lithiation/delithiation behavior. The carbon-coated β -Si₃N₄/Si is mixed with artificial graphite (AG) to fabricate a composite anode. Full cells using LiNi_{0.8}Co_{0.1}Mn_{0.1}O₂ cathodes are constructed and their charge–discharge performance is evaluated. The incorporation of the proposed carbon-coated β -Si₃N₄ is shown to significantly enhance the rate capability and cyclability of Si anodes for next-generation LIBs.

2. Results and Discussion

The crystallinity of the carbon-coated α -Si₃N₄ (denoted as C- α -Si₃N₄) and carbon-coated β -Si₃N₄ (denoted as C- β -Si₃N₄) was examined using XRD; the obtained diffraction patterns are shown in Figure S1, Supporting Information. The peaks at 20.6°, 22.9°, 26.5°, 31.0°, 34.6°, and 35.3° are respectively indexed as (101), (110), (200), (201), (102), and (210) plane diffraction of trigonal α -Si₃N₄ (JCPDS-41-0360). The peaks at 13.4°, 23.4°, 27.1°, 33.7°, 36.1°, and 41.4° are associated with the (100), (110), (200), (101), (210), and (201) plane diffraction of hexagonal β -Si₃N₄ (JCPDS-33-1160). The α phase was determined to have the lattice parameters $a = b = 7.766(2)$ Å and $c = 5.615(3)$ Å, whereas the β phase had the lattice parameters $a = b = 7.586(2)$ Å and $c = 2.902(1)$ Å. In each Si₃N₄ sample, the other allotrope appeared as a minor fraction; specifically, the α -Si₃N₄ sample had $\approx 2\%$ β -Si₃N₄ and the β -Si₃N₄ sample had $\approx 7\%$ α -Si₃N₄. No other impurity phases were detected. Due to the low crystallinity of the carbon layers, no distinct diffraction signal was observed. Figure 1a shows the Raman spectra of the α -Si₃N₄, β -Si₃N₄, C- α -Si₃N₄, and C- β -Si₃N₄ samples. Both carbon-coated samples exhibit a D-band signal at ≈ 1345 cm⁻¹ and a G-band signal at ≈ 1595 cm⁻¹. The former is associated with imperfect carbon bonding and the latter originates from the Raman-allowed in-plane vibration of sp² carbon. The D-to-G-band intensity ratio (I_D/I_G) is a critical index that reflects the graphitization degree of carbon materials. The I_D/I_G ratios of C- α -Si₃N₄ and C- β -Si₃N₄ are ≈ 1.1 , indicating that the deposited carbon was amorphous.^[39,40] The carbon content of the samples was quantitatively evaluated with TGA; the data are shown in Figure 1b. Both the C- α -Si₃N₄ and C- β -Si₃N₄ samples underwent clear weight loss at around 550–680 °C, which was associated with the burnout of the carbon layers. The data indicate that α -Si₃N₄ and β -Si₃N₄ have great thermal stability and that the carbon content of both coated samples is approximately 10 wt.%. Figure 1c–f shows Scanning electron microscopy (SEM) images of α -Si₃N₄, β -Si₃N₄, C- α -Si₃N₄, and C- β -Si₃N₄ powders, respectively. Irregularly granular morphologies were observed for all

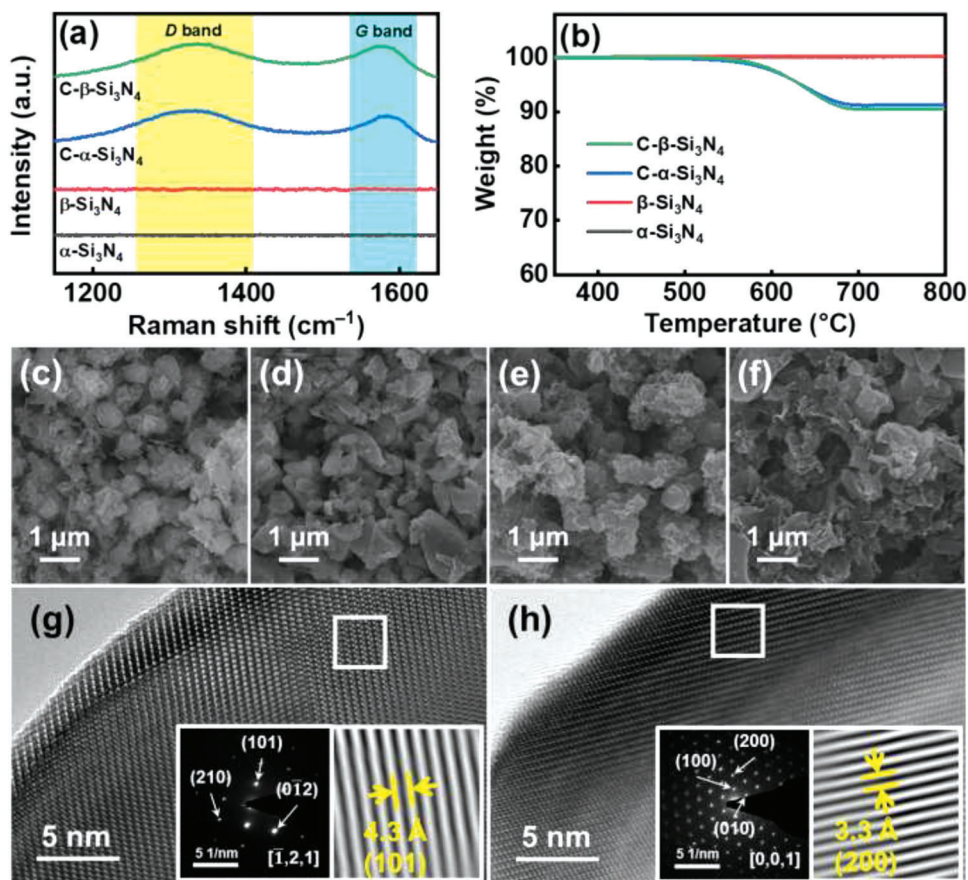


Figure 1. a) Raman spectra, b) TGA data, SEM images of c) α - Si_3N_4 , d) β - Si_3N_4 , e) C- α - Si_3N_4 , and f) C- β - Si_3N_4 , and high-resolution TEM images of g) α - Si_3N_4 and h) β - Si_3N_4 .

samples. Figure 1g,h respectively shows high-resolution lattice images of α - Si_3N_4 and β - Si_3N_4 particles, which reveal that both allotropes are highly crystalline. The lattice fringes with spacings of 4.3 and 3.3 Å are associated with the (101) and (200) plane distances of the α - Si_3N_4 and β - Si_3N_4 crystals, respectively. The electron diffraction patterns shown in the figure insets confirm the phase identification results obtained from XRD.

Figure 2a–d shows the initial charge–discharge curves of various electrodes measured at a current rate of 0.05 A g^{-1} . The initial Coulombic efficiency (CE) values of the α - Si_3N_4 , β - Si_3N_4 , C- α - Si_3N_4 , and C- β - Si_3N_4 electrodes are 43%, 52%, 54%, and 57%, respectively. The efficiency loss is ascribed to SEI formation and the irreversible trapping of Li^+ ions within the electrodes. The carbon coating improved electron and Li^+ conduction, thus increasing CE and the measured capacities. The intrinsic electronic conductivity values of α - Si_3N_4 and β - Si_3N_4 are $\approx 10^{-13} \text{ S cm}^{-1}$.^[41,42] After carbon coating, the values increase to 1.02×10^{-1} and $1.07 \times 10^{-1} \text{ S cm}^{-1}$, respectively (Table S1, Supporting Information). Figure 2e–h shows the electrode charge–discharge profiles recorded at various current rates after two conditioning cycles. The reversible capacities obtained at 0.05 A g^{-1} are 80, 91, 109, and 118 mAh g^{-1} for the α - Si_3N_4 , β - Si_3N_4 , C- α - Si_3N_4 , and C- β - Si_3N_4 electrodes, respectively. With increasing current rate, the specific capacities decreased, as shown in Table S2, Supporting Information. The capacities decreased to 31, 42,

52, and 62 mAh g^{-1} , respectively, at a specific current of 2 A g^{-1} , corresponding to 39%, 46%, 48%, and 53% of the capacities found at 0.05 A g^{-1} . This is the first electrochemical performance comparison between two Si_3N_4 allotropes. The superior charge–discharge properties of β - Si_3N_4 could be associated with β - Si_3N_4 having continuous *c*-axis channels that are approximately 300 pm in diameter, which could benefit Li^+ transport owing to the wide space between basal layers constituted by the linking of six eight-member Si-N rings.^[33,38] In contrast, for α - Si_3N_4 , because of the existence of a *c* glide plane, the continuous channels are interrupted, and thus a series of interstices form,^[33] which is unfavorable for Li^+ conduction. Figure 2i shows the electrochemical impedance spectroscopy (EIS) data of various electrodes acquired after two conditioning cycles. The Nyquist spectra consist of a semicircle at high frequency and a sloping line at low frequency, which can be characterized by the equivalent circuit shown in the figure inset, where R_e , R_{ct} , CPE, and W represent the electrolyte resistance, charge transfer resistance, interfacial constant-phase element, and Warburg impedance associated with Li^+ diffusion within the electrode, respectively.^[43] The R_{ct} values derived from the data fitting are 44, 39, 34, and 31 Ω for the α - Si_3N_4 , β - Si_3N_4 , C- α - Si_3N_4 , and C- β - Si_3N_4 electrodes, respectively. The apparent Li^+ diffusion coefficient ($D_{\text{Li}^+}^{\text{(EIS)}}$) can be estimated from the EIS sloping line in the low-frequency region.^[44] The calculated $D_{\text{Li}^+}^{\text{(EIS)}}$ values for the four electrodes are 2.6, 3.1, 6.1, and

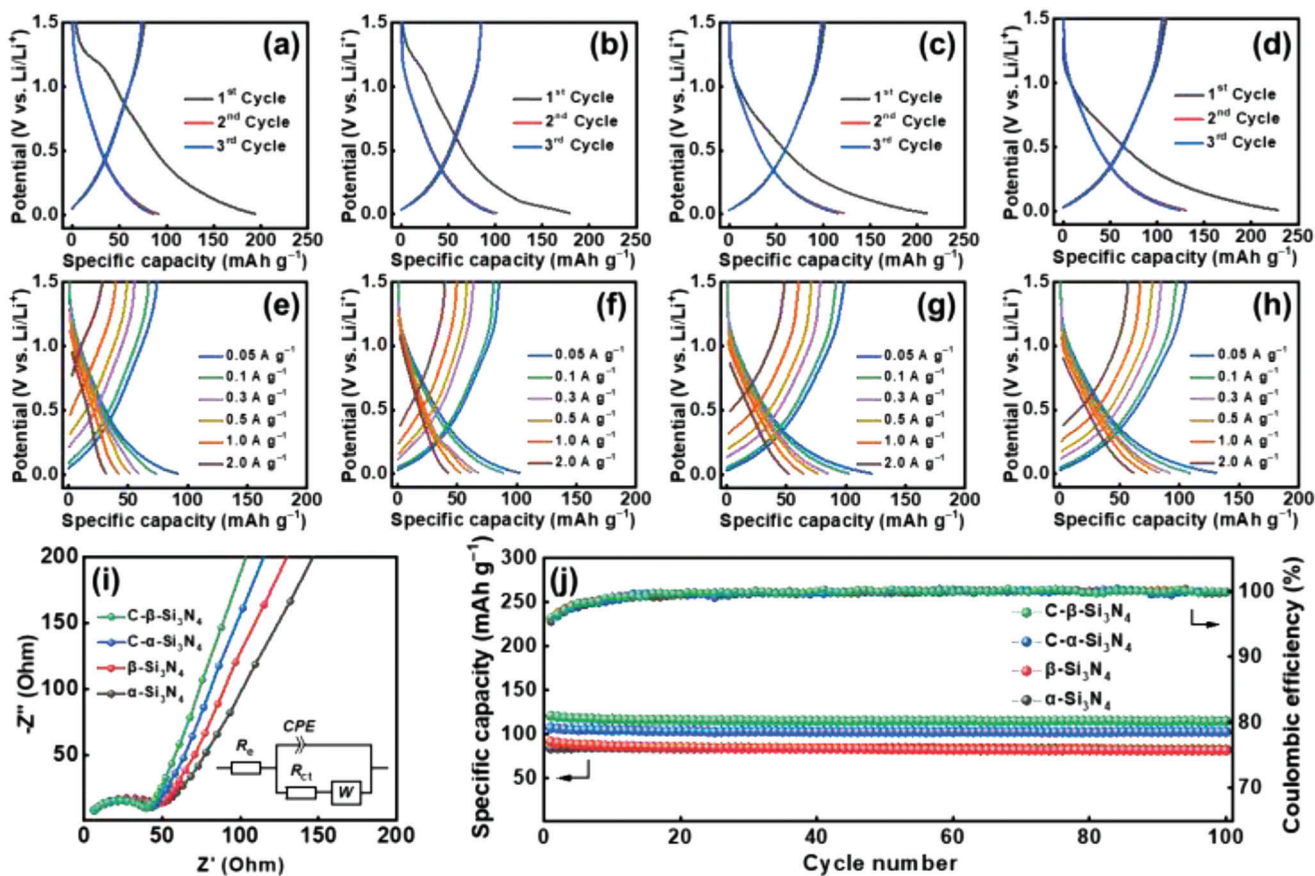


Figure 2. Charge–discharge curves of a,e) α - Si_3N_4 , b,f) β - Si_3N_4 , c,g) C- α - Si_3N_4 , and d,h) C- β - Si_3N_4 electrodes. i) EIS data of various electrodes and equivalent circuits used for data fitting. j) Cycling stability of various electrodes measured at 0.05 A g^{-1} .

$6.9 \times 10^{-14} \text{ cm}^2 \text{ s}^{-1}$, respectively. Both the R_{ct} and D_{Li^+} data support C- β - Si_3N_4 having the best high-rate performance among the electrodes. Figure 2j shows the cycling stability data of the electrodes measured at 0.05 A g^{-1} . All the electrodes are highly stable over cycling, with the capacity retention being above 95% and the saturated CE values being above 99.9%. Because C- β - Si_3N_4 had the best performance, it was used for further analyses.

Next, we attempted to integrate β - Si_3N_4 and Si with various weight ratios using high-energy ball milling. Figure 3a shows the Raman spectra of various samples. The peak, which is related to the vibration band of polycrystalline Si,^[32] shifts from 520 to 515 cm^{-1} with increasing β - Si_3N_4 fraction. This is associated with Si lattice distortion and the formation of an interface in the composites.^[32,45] Figure 3a also shows the carbon D and G bands for all the C- β - Si_3N_4 /Si samples, confirming that the carbon coating was successfully deposited. According to the TGA data in Figure 3b, the carbon content of all the samples was approximately $\approx 10 \text{ wt.}\%$. Figure 3c shows the results of the dynamic light scattering (DLS) measurements. According to the particle size distribution profiles, the D_{50} values of C- β - Si_3N_4 , C- β - Si_3N_4 /25%Si, C- β - Si_3N_4 /50%Si, C- β - Si_3N_4 /75%Si, and C-Si are 588, 496, 375, 307, and 210 nm, respectively. It is noted that only a single DLS peak was observed for all the samples. These results suggest that the β - Si_3N_4 and Si phases were well integrated, creating a homogeneous composite. Figure S2, Supporting In-

formation, shows the XRD patterns of various samples, confirming the dual-phase nature of the β - Si_3N_4 /Si composites without the formation of new compounds after mixing. Table S3, Supporting Information, shows the tap densities of the samples. As shown, a higher β - Si_3N_4 fraction led to higher density. A denser material is essential for making a more compact electrode, which is favorable for electrode volumetric performance.^[46] Figure 3d shows high-resolution transmission electron microscopy (TEM) images of the C- β - Si_3N_4 /50%Si sample. As shown, the carbon coating is about $\approx 5 \text{ nm}$ in thickness and the two phases are integrated. The phase boundary between Si and β - Si_3N_4 is marked in the figure. The lower part of the particle is a Si phase domain, as confirmed by the electron diffraction pattern shown in the figure inset. The observed d spacing of 3.1 \AA is attributed to the Si (111) plane distance. The upper part of the particle is identified as polycrystalline β - Si_3N_4 . The three distinct positions marked in the figure have d spacing values of 3.3, 2.7, and 2.5 \AA , corresponding to the (200), (101), and (210) planes of β - Si_3N_4 , respectively.

The corrosion resistance of the C- β - Si_3N_4 , C- β - Si_3N_4 /50%Si, and C-Si to HF were evaluated. The samples were immersed in 25 mM HF aqueous solution at $25 \text{ }^\circ\text{C}$ for 1 h, and the weight loss data are shown in Figure S3, Supporting Information. It is confirmed that the dissolution rate of C- β - Si_3N_4 is much lower than that of C-Si.

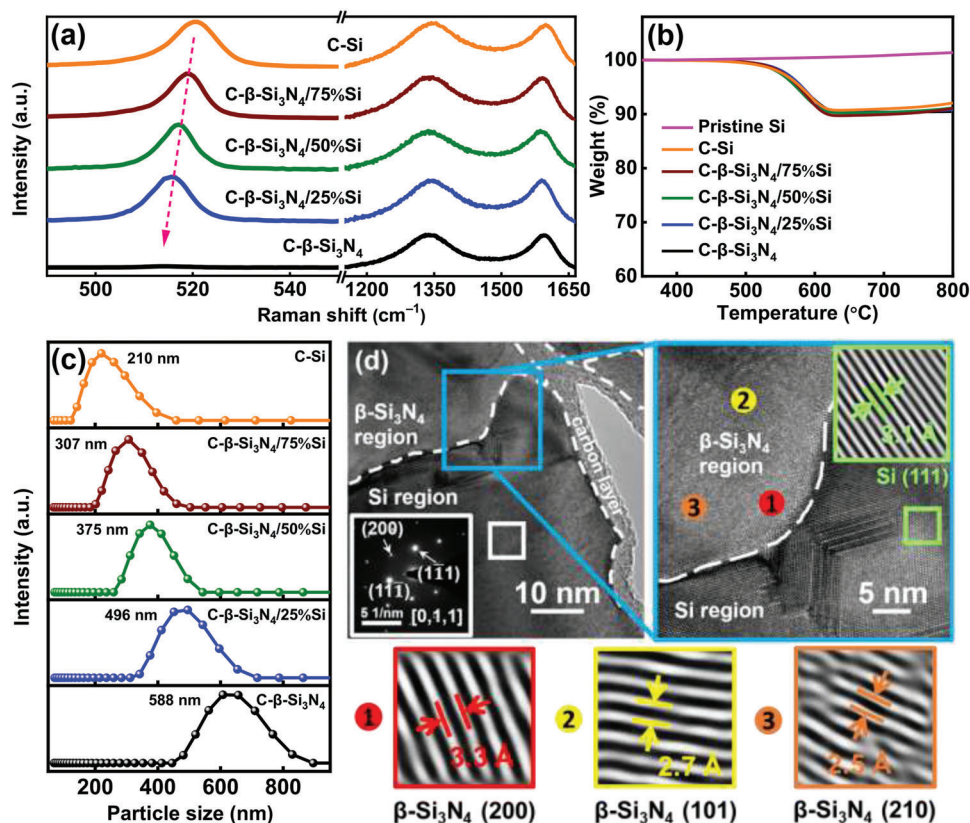


Figure 3. a) Raman spectra, b) TGA data, and c) particle size distribution of various samples. d) High-resolution TEM images of C- β -Si₃N₄/50%Si sample.

Figure 4a shows the X-ray photoelectron spectroscopy (XPS) Si 2p spectra of the C- β -Si₃N₄, C- β -Si₃N₄/25%Si, C- β -Si₃N₄/50%Si, and C- β -Si₃N₄/75%Si samples, respectively. The spectra can be split into four peaks: Si-Si at 99.2 eV, Si-N at 102.3 eV, Si-O at 103.3 eV, and O-Si-O at 105.0 eV.^[8,30] With increasing Si phase fraction, the Si-Si, Si-O, and O-Si-O intensities monotonically increase, indicating that the Si (rather than β -Si₃N₄) particle surface is relatively oxygen-enriched. The C 1s spectra of the samples are shown in Figure 4b. Higher C-O (at 286.2 eV) and O=C=O (at 288.7 eV) concentrations are found for the sample with a higher Si phase content. It is noted that the C-N-O bonds become intensified when the β -Si₃N₄ fraction increases. The N 1s spectra presented in Figure 4c can be deconvoluted into three components. The distinctive peaks at 397.7, 398.5, and 400.9 eV are associated with Si-N, N-Si-O, and pyrrolic nitrogen, respectively. The existence of pyrrolic nitrogen implies that the nitrogen from the milled β -Si₃N₄ could diffuse into the carbon layers. The N-Si-O is supposed to be a new species that formed at the β -Si₃N₄/Si interface. Figure 4d shows the O 1s spectra, which are split into two peaks, namely O-C and O-Si peaks at 532.0 and 532.9 eV, respectively. The intensity of the latter peak increases with Si phase fraction, which can be explained by Si being intrinsically active and easily oxidized^[47,48] during synthesis (see Experimental section for details).

To study the electrochemical properties of various electrodes, CV measurements were performed. Figure S4a-e, Supporting Information, shows the obtained CV curves of the C- β -Si₃N₄, C- β -

Si₃N₄/25%Si, C- β -Si₃N₄/50%Si, C- β -Si₃N₄/75%Si, and C-Si electrodes, respectively. The cathodic peaks at \approx 1.2 V for all electrodes can be assigned to the reductive decomposition of the electrolyte and the formation of SEI layers.^[49,50] For the C- β -Si₃N₄ electrode, there is a clear redox current below \approx 0.5 V, indicating that β -Si₃N₄ is not completely inert. Some conversion and/or intercalation reactions may be involved (discussed later). However, bulk transformation from β -Si₃N₄ to Si did not happen because no visible Si alloying/dealloying CV characteristics were found. The XRD and XPS data in Figure S5, Supporting Information, further support that there is no formation of Si phase after the CV scans. As shown, with increasing Si phase fraction in the electrodes, the redox signals of Si become more pronounced. The reduction peaks at \approx 0.2 V and below 0.1 V can be ascribed to the evolution of various Li-Si alloy phases.^[8] Upon the anodic scan, two distinct peaks emerged at 0.38 and 0.51 V, which correspond to the phase transition from Li₁₅Si₄ to amorphous Li_xSi and that from amorphous Li_xSi to Si, respectively.^[51] During consecutive scans, the CV current increased, reflecting the electrode activation process toward lithiation/delithiation.^[52,53]

Figure S6a-d, Supporting Information, shows the initial three charge-discharge cycles of various electrodes measured at 0.2 A g⁻¹. The first-cycle CE values of the C- β -Si₃N₄/25%Si, C- β -Si₃N₄/50%Si, C- β -Si₃N₄/75%Si, and C-Si electrodes are 65%, 78%, 83%, and 86%, respectively. Some irreversible redox reactions were involved for β -Si₃N₄, leading to a lower initial CE for the electrode with a higher β -Si₃N₄ fraction. As shown in Figure

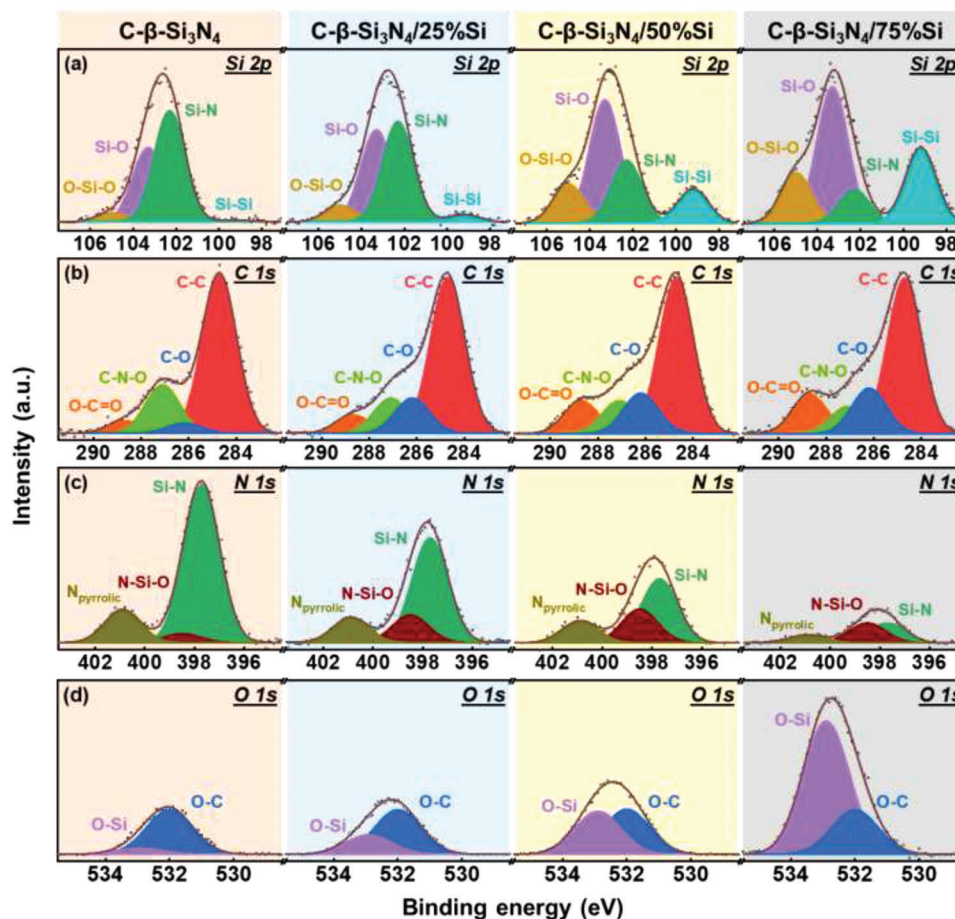


Figure 4. XPS a) Si 2p, b) C 1s, c) N 1s, and d) O 1s spectra of various samples.

S6, Supporting Information, when the Si fraction exceeded 50%, the delithiation (defined as discharge in this study) capacity decay upon cycling was pronounced. This suggests that β -Si₃N₄ can help stabilize electrode performance. Figure 5a–d shows the charge–discharge profiles of the electrodes measured at various rates after two conditioning cycles. The reversible capacities obtained at 0.2 A g^{−1} are 583, 1068, 1390, and 1820 mAh g^{−1} for the C- β -Si₃N₄/25%Si, C- β -Si₃N₄/50%Si, C- β -Si₃N₄/75%Si, and C–Si electrodes, respectively. As shown in Figure 5e and Table 1, the specific capacities of these electrodes decrease to 250, 488, 452, and 437 mAh g^{−1}, respectively, at a specific current of 5 A g^{−1}, corresponding to 43%, 46%, 33%, and 24% retention compared to the capacities found at 0.2 A g^{−1}. Figure 5f shows the EIS data of the electrodes acquired after the conditioning cycles. The R_{ct} values are 13, 10, 20, and 42 Ω for C- β -Si₃N₄/25%Si, C- β -Si₃N₄/50%Si, C- β -Si₃N₄/75%Si, and C–Si, respectively (Table 2). The Li⁺ transport properties within the electrodes were evaluated using the galvanostatic intermittent titration technique (GITT).^[54] The results are shown in Figure S7, Supporting Information, and the calculated average D_{Li^+} values ($D_{Li^+}^{(GITT)}$) are summarized in Table 2. As shown, the C- β -Si₃N₄/50%Si electrode has the highest $D_{Li^+}^{(GITT)}$ values of 4.6 and 5.1×10^{-10} cm² s^{−1}, for lithiation and delithiation, respectively. The favorable R_{ct} and $D_{Li^+}^{(GITT)}$ values explain the optimal rate

capability of the C- β -Si₃N₄/50%Si electrode. The expected capacities of various C- β -Si₃N₄/Si composite anodes can be calculated from the linear combination of the measured capacities of the C- β -Si₃N₄ and C–Si electrodes, as shown in Table S4, Supporting Information. As shown, the real capacities of C- β -Si₃N₄/Si composite anodes are higher than the expected values, confirming that synergistic effects happen, especially at high rates. It is noted that the strongest synergy is found for the C- β -Si₃N₄/50%Si electrode. The Si phase was modified (Figure 3a) by the incorporation of β -Si₃N₄. However, a high β -Si₃N₄ fraction led to a lower electronic conductivity of the composite (Table S1, Supporting Information). Moreover, the created interface between Si and β -Si₃N₄ may favor Li⁺ transport. There is thus an optimal β -Si₃N₄-to-Si ratio that maximizes electrode performance.

Figure 5g shows the cycling stability data of various electrodes measured at 1 A g^{−1}. The steady CE values are 99.9%, 99.9%, 99.8%, and 99.7% for the C- β -Si₃N₄/25%Si, C- β -Si₃N₄/50%Si, C- β -Si₃N₄/75%Si, and C–Si electrodes, respectively. After 300 charge–discharge cycles, the electrodes retained 84%, 75%, 30%, and 15% of their initial capacities, respectively. A satisfactory cycling stability can be achieved with a Si fraction of up to 50%. The specific capacity of 700 mAh g^{−1} for C- β -Si₃N₄/50%Si is the highest value among the electrodes studied after 300 cycles. As shown in Table S5, Supporting Information, this durability

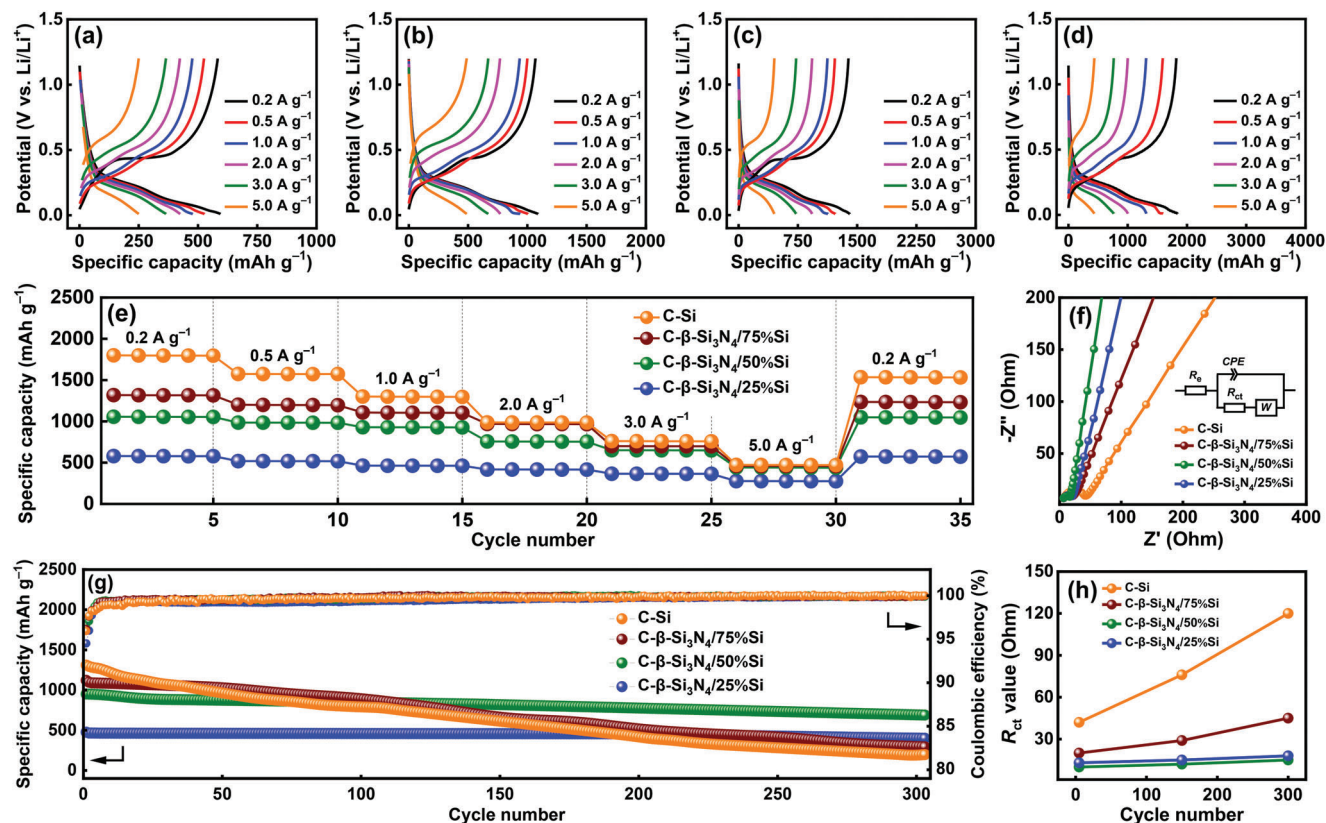


Figure 5. Charge–discharge profiles of a) C-β-Si₃N₄/25%Si, b) C-β-Si₃N₄/50%Si, c) C-β-Si₃N₄/75%Si, and d) C-Si electrodes measured at various rates. e) Comparative rate performance of various electrodes. f) EIS spectra of various electrodes. g) Cycling stability of various electrodes measured at 1 A g⁻¹. h) Variation of R_{ct} values of various electrodes with respect to charge–discharge cycle number.

Table 1. Reversible specific capacities of C-β-Si₃N₄/25%Si, C-β-Si₃N₄/50%Si, C-β-Si₃N₄/75%Si, and C-Si electrodes measured at various specific currents.

Current rate [A g ⁻¹]	C-β-Si ₃ N ₄ /25%Si [mAh g ⁻¹]	C-β-Si ₃ N ₄ /50%Si [mAh g ⁻¹]	C-β-Si ₃ N ₄ /75%Si [mAh g ⁻¹]	C-Si [mAh g ⁻¹]
0.2	583	1068	1390	1820
0.5	525	1000	1218	1591
1	476	935	1124	1311
2	424	769	930	1001
3	365	670	728	765
5	250	488	452	437
High rate retention ^{a)}	43%	46%	33%	24%

^{a)} a comparison between reversible capacities at 5 and 0.2 A g⁻¹.

is comparable to the best performance reported in the literature. The impedance evolution of the electrodes after cycling was also investigated (see Figure S8, Supporting Information). As shown in Figure 5h, the R_{ct} values clearly increase upon cycling when the Si phase fraction is more than 50%. The postmortem SEM images of various electrodes after cycling are shown in Figure S9, Supporting Information. The morphologies of the C-β-Si₃N₄/75%Si and C-Si electrodes were clearly distorted compared to those of the pristine electrodes. The Si particles signif-

Table 2. R_{ct} and D_{Li⁺}(GITT) values of various electrodes measured after conditioning cycles.

Samples	R _{ct} [Ω]	D _{Li⁺} (GITT) for lithiation/delithiation [× 10 ⁻¹⁰ cm ² s ⁻¹]
C-β-Si ₃ N ₄ /25%Si	13	3.7/4.8
C-β-Si ₃ N ₄ /50%Si	10	4.6/5.1
C-β-Si ₃ N ₄ /75%Si	20	3.1/4.2
C-Si	42	2.5/3.3

icantly expanded and agglomerated. Moreover, both electrodes were covered by thick SEI layers, leading to increased R_{ct} and capacity deterioration. In contrast, an adequate fraction of β-Si₃N₄ (i.e., ≥50%) is beneficial for preserving the electrode structural stability during repeated lithiation/delithiation. Figure S10, Supporting Information, shows the cross-section SEM images of the C-β-Si₃N₄/50%Si and C-Si electrodes before and after 25 charge–discharge cycles. Much less volume expansion and better integrity of the former electrode are confirmed.

To gain more insight into the SEI chemistry, XPS analyses were performed for the C-β-Si₃N₄/50%Si and C-Si electrodes after two conditioning cycles. As shown by the Si 2p orbital data in Figure 6, a new Si₃N_{4-x} species formed for the C-β-Si₃N₄/50%Si electrode, suggesting that the nitrogen in β-Si₃N₄ was consumed.

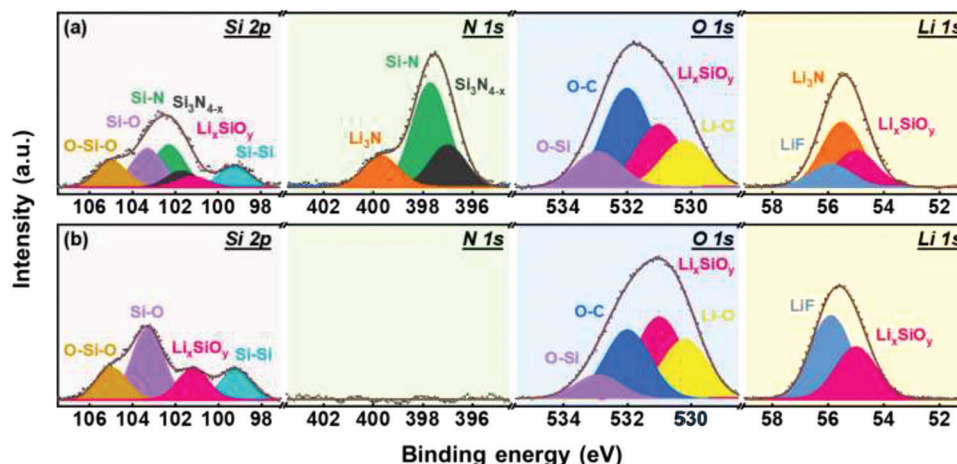


Figure 6. XPS Si 2p, N 1s, O 1s, and Li 1s spectra of a) C- β -Si₃N₄/50%Si and b) C-Si electrodes after conditioning cycles.

In addition, Li_xSiO_y was found to be a compound in both SEI layers. The N 1s spectrum indicates the formation of Li₃N^[55,56] on the C- β -Si₃N₄/50%Si electrode. Upon lithiation, Li⁺ ions reacted with the nitrogen in β -Si₃N₄ to form Li₃N, leaving behind Si₃N_{4-x}. Of note, Li₃N is a highly favorable SEI component that can provide high mechanical robustness, great passivation ability, and high Li⁺ conductivity.^[57–59] In the O 1s spectra, four constituents were observed, namely Li–O, Li_xSiO_y, O–C, and O–Si. The C–Si surface is relatively Li–O- and Li_xSiO_y-enriched, implying that the SEI layer is thicker than that on the C- β -Si₃N₄/50%Si electrode. Based on the Li 1s spectra, the SEI on C- β -Si₃N₄/50%Si has high Li₃N content, whereas that of C–Si is composed of LiF and Li_xSiO_y. The much higher Li⁺ conductivity of Li₃N^[60] compared to that of LiF explains the superior rate capability of the C- β -Si₃N₄/50%Si electrode. Figure S11, Supporting Information, shows the XPS analysis data of the C- β -Si₃N₄/50%Si electrode after 300 charge–discharge cycles. As shown, the surface chemical composition is close to that of the electrode before cycling (Figure 6a). This indicates that the Li₃N-containing SEI, derived from β -Si₃N₄, is stable and robust against long cycling.

Figure 7a,b shows operando XRD data of the C- β -Si₃N₄/50%Si and C–Si electrodes, respectively, during the initial two charge–discharge cycles. As shown in Figure 7c, the diffraction intensity of β -Si₃N₄ of the former electrode decreases during lithiation, confirming that β -Si₃N₄ is partially consumed and not completely inactive. However, the crystalline structure of β -Si₃N₄ is preserved. Even after 300 cycles, as shown in the high-resolution TEM image in Figure S12, Supporting Information, the β -Si₃N₄ crystals can be clearly observed. The β -Si₃N₄ nanoparticles seem to be embedded in the matrix of amorphous Si and SEI. Also shown in Figure 7c is the high reversibility of Li₁₅Si₄ formation and dissolution upon cycling. The Si peak intensity decreases at the first lithiation but becomes more stable at the second lithiation. The introduction of β -Si₃N₄ seems to stabilize the Si phase and thus alleviates the strong Li⁺ uptake reactions. Therefore, the electrode cyclability is improved. In contrast, as shown in Figure 7d (for the C–Si electrode), the Si intensity continuously and substantially fades upon cycling. Moreover, the Li₁₅Si₄ intensity at the second cycle is considerably higher than that at the

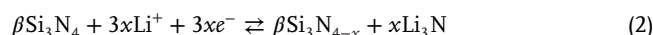
first cycle, indicating that the Li⁺ uptake reactions, and thus the material volume change, were aggravated.

The crystal size (*L*) of the Si, β -Si₃N₄, and Li₁₅Si₄ phases at various states of charge can be estimated using Scherrer's formula:^[61]

$$L = \frac{K \times \lambda}{B \cos \theta} \quad (1)$$

where *K* is the Scherrer constant, which can be considered to be 0.94 for spherical crystallites, λ is the X-ray wavelength, and *B* is the full width at half maximum of the XRD peak at a diffraction angle of 2 θ . The calculation results are shown in Figure 7e,f. The β -Si₃N₄ crystal size slightly decreases during lithiation, confirming that the crystal is indeed consumed. With the incorporation of β -Si₃N₄, the crystal size of Li₁₅Si₄ markedly decreases and the size variation upon lithiation and delithiation becomes more reversible compared to that of the C–Si electrode. It has been reported that a smaller Li₁₅Si₄ crystal size leads to improved electrode cycle life.^[62,63] The crystal size of Si was found to be decreased when the β -Si₃N₄ was introduced. However, as shown, the Si crystal size reduction upon cycling was somewhat mitigated. For the C–Si electrode, the Si crystal size significantly decreased and became nearly amorphous after two cycles. The operando XRD data confirm that the incorporated β -Si₃N₄ indeed alters the phase evolution behavior of the electrode during charging and discharging.

Figure 8 shows the structure evolutions of the C- β -Si₃N₄/50%Si and C–Si electrodes. The former sample is coated by an N-containing carbon layer (confirmed by the XPS pyrrolic nitrogen and C–N–O signals). The N doping increases the electronic conductivity and electrolyte affinity of the carbon layer.^[64] This is crucial for compensating for the low electronic conductivity of β -Si₃N₄, which is partially consumed via the following conversion reaction:



This reaction could be partially reversible. Besides, some shallow Li⁺ intercalation reactions and double-layer charging reactions could take place, contributing to the measured capacity of

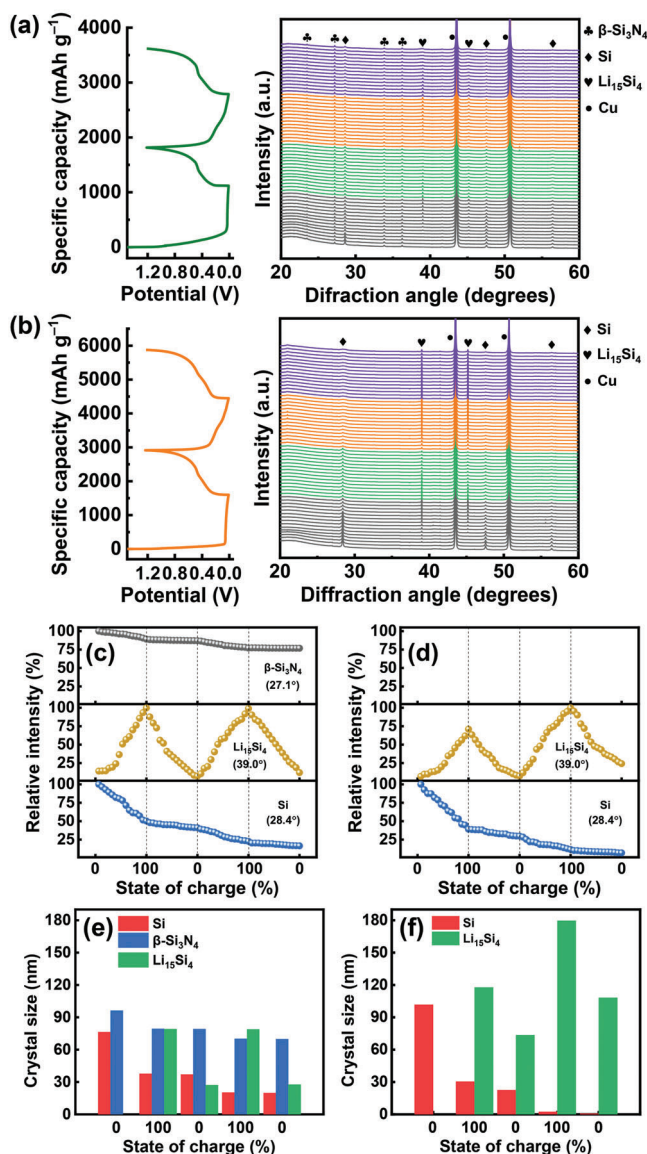


Figure 7. Operando XRD data of a) C- β -Si₃N₄/50%Si and b) C-Si electrodes during initial two charge–discharge cycles. Relative peak intensity versus state of charge of c) C- β -Si₃N₄/50%Si and d) C-Si electrodes. Crystal size variation of Si, β -Si₃N₄, and Li₁₅Si₄ in e) C- β -Si₃N₄/50%Si and f) C-Si electrodes.

β -Si₃N₄. Upon cycling, β -Si₃N₄ helps mechanically stabilize the electrode structure. As shown in the enlarged image, even though a Si₃N_{4-x} species formed, the crystalline structure of hexagonal β -Si₃N₄ was preserved, alleviating the electrode volume variation. The formed Li₃N at the β -Si₃N₄/Si interface establishes a percolating Li⁺ conducting network across the composite electrode. In addition, due to the high robustness and good passivation ability of Li₃N, the surface SEI layer is thin and stable. It is believed that there is a distorted Si layer (based on Raman data) with N and O content (based on XPS data) near the β -Si₃N₄/Si interface that has relatively low activity toward Li⁺ uptake (i.e., low volume expansion). This layer can thus be a buffer intermediate that ac-

commodates the strain generated at the interface, increasing electrode cyclability. In contrast, a conventional C-Si electrode has large volume variation during cycling. Thus, cracks easily form and particle pulverization occurs. The repeated breakdown and formation of the SEI lead to its continuous accumulation, which increases the Li⁺ transport distance and hinders the charge transfer reactions. Moreover, the thickened SEI gradually isolates the loosely connected Si and carbon fragments, causing rapid capacity deterioration.

Next, AG was incorporated into C- β -Si₃N₄/50%Si with a weight ratio of 1:1. The corresponding charge–discharge profiles are shown in **Figure 9**. The C- β -Si₃N₄/50%Si@AG electrode has reversible capacities of 849, 697, and 396 mAh g⁻¹ at 0.2, 1, and 5 A g⁻¹, respectively. **Figure 9c** shows the cycling stability data of the C- β -Si₃N₄/50%Si@AG electrode measured at 1 A g⁻¹. The steady CE value reached >99.9%. After 300 charge–discharge cycles, the electrode retained a capacity of 628 mAh g⁻¹, corresponding to 90% of the initial capacity. As shown in Table S5, Supporting Information, this is among the best electrode durability values reported in the literature. C- β -Si₃N₄/50%Si||NMC-811 and C- β -Si₃N₄/50%Si@AG||NMC-811 cells were assembled for the evaluation of full-cell properties. **Figure S13**, Supporting Information, shows the obtained charge–discharge curves of the cells measured at various C rates. The gravimetric energy densities of the two cells based on the total mass of negative and positive electrode active materials are estimated to be \approx 575 and \approx 560 Wh kg⁻¹, respectively, at 0.1 C. This reveals the merits of the proposed C- β -Si₃N₄/Si-based composite anodes.

3. Conclusions

The superior lithiation/delithiation properties of β -Si₃N₄ over α -Si₃N₄ were confirmed. β -Si₃N₄/Si composites were synthesized via a facile ball-milling method and a simple wet chemical protocol was used to form an N-containing carbon coating, where the nitrogen originated from β -Si₃N₄. In contrast to the traditional understanding of crystalline Si₃N₄, which was thought to be electrochemically inactive, we found that the incorporated β -Si₃N₄ substantially alters the charge–discharge performance of Si electrodes. The strongest synergistic effects of combining β -Si₃N₄ and Si phases on the specific capacities were found for the C- β -Si₃N₄/50%Si electrode. Of note, the N-containing carbon-coated β -Si₃N₄ moderately participated in the lithiation reactions. β -Si₃N₄ was partially consumed (leaving behind Si₃N_{4-x}) to form Li₃N, which is protective and highly Li⁺ conductive, both on the electrode surface and at the β -Si₃N₄/Si interface. However, the crystalline structure of the hexagonal β -Si₃N₄ was well preserved even after prolonged cycling, which mechanically stabilized the electrode, prevented Si particle agglomeration, and thus suppressed capacity degradation. Operando XRD results confirmed that with the incorporation of β -Si₃N₄, the crystal size of Li₁₅Si₄ considerably decreased and the Li₁₅Si₄ formation and dissolution upon lithiation/delithiation became more reversible. Moreover, there is a distorted Si layer with N and O content near the β -Si₃N₄/Si interface that has relatively low activity toward Li⁺ uptake (i.e., low volume expansion). This layer can be an intermediate to buffer the volume variation of the bulk Si phase, increasing electrode cyclability. The C- β -Si₃N₄/50%Si@AG electrode showed a reversible capacity of 849 mAh g⁻¹ at 0.2 A g⁻¹.

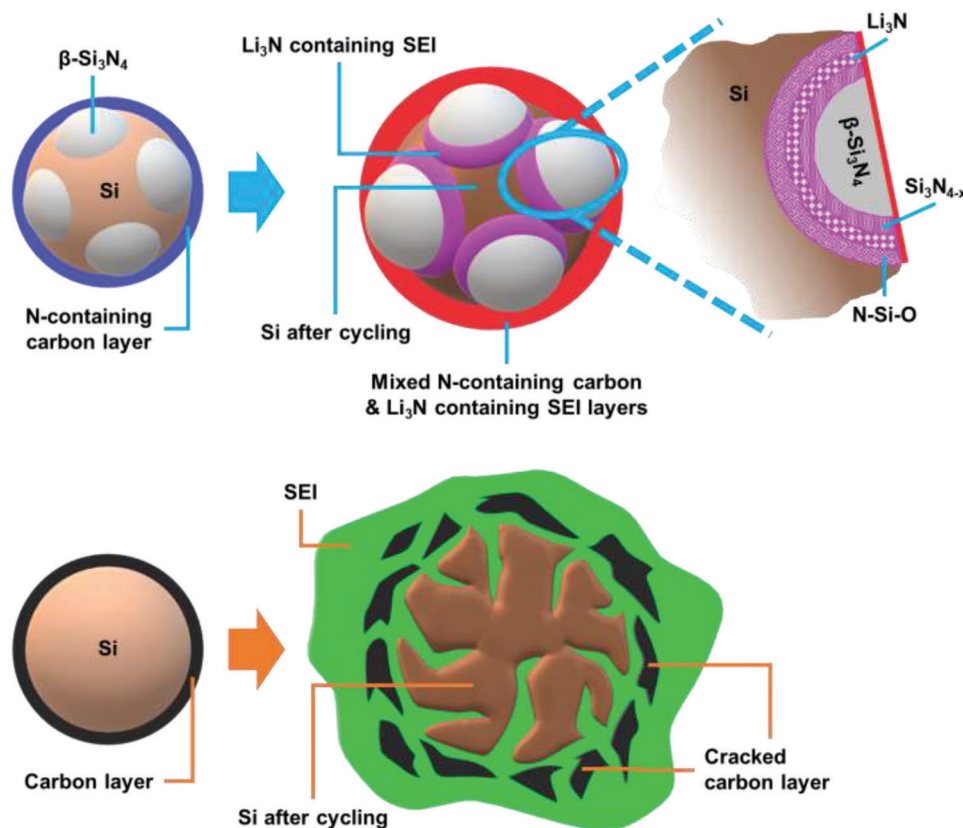


Figure 8. Schematic illustration of structure evolution in C- β -Si₃N₄/50%Si and C-Si electrodes after charge–discharge cycling.

After 300 cycles, this electrode retained 90% of its initial capacity with a steady CE value of above 99.9%. In addition, the C- β -Si₃N₄/50%Si||NMC-811 and C- β -Si₃N₄/50%Si@AG||NMC-811 full cells showed promising energy densities of ≈ 575 and ≈ 560 Wh kg⁻¹ (based on active materials), respectively. The unique role of β -Si₃N₄ in the enhancement of the electrochemical performance of Si-based anodes was examined. The great potential for high-energy-density and high-reliability LIB applications is expected.

4. Experimental Section

Synthesis of Carbon-Coated α -Si₃N₄, β -Si₃N₄, and β -Si₃N₄/Si Composites: Commercial Si powder, α -Si₃N₄ powder, and β -Si₃N₄ powder were provided by Super Energy Material Inc., Taiwan. AG (D_{50} : ≈ 16 μ m, purity: >99.9%) was purchased from Shanghai Shanshan Technology Co. Ltd. β -Si₃N₄/Si composites with various β -Si₃N₄-to-Si ratios were prepared via high-energy ball milling. Briefly, β -Si₃N₄ and Si powders at various weight ratios (β -Si₃N₄/Si = 25/75, 50/50, 75/25) were dispersed in anhydrous ethanol and transferred to a zirconia vessel for planetary ball milling (a powder/zirconia ball weight ratio of 1/10 was used). A carbon coating was applied to various powders using a wet chemical method.^[65] In this process, glucose was used as the carbon precursor and the carbonization was performed at 850 °C under Ar for 5 h.

Cell Assembly: The anode active material, Super P, and sodium polyacrylate binder were mixed in a 7:2:1 ratio with deionized water. The slurry was cast onto Cu foil using a doctor blade and then vacuum-dried at 100 °C for 6 h. The obtained electrode was punched to match the required di-

mensions of a CR2032 coin cell. The active material mass loading was ≈ 2 mg cm⁻². Li foil and a glass fiber membrane were used as the counter electrode and separator, respectively. For the full cell construction, the developed anode was paired with a LiNi_{0.8}Mn_{0.1}Co_{0.1}O₂ (NMC-811) cathode with an anode-to-cathode capacity ratio of 1.15:1. The anode was pre-conditioned for two cycles in half cells prior to the full cell assembly. An electrolyte composed of 1 M LiPF₆ salt, ethylene carbonate/diethyl carbonate mixed solvent (1:1 by volume), and 5 wt.% fluoroethylene carbonate additive was adopted. The coin cells were assembled in an Ar-filled glove box (Vigor Tech. Co. Ltd.), where both the moisture and oxygen content levels were maintained below 0.1 ppm.

Material and Electrochemical Characterizations: The crystallinity of the samples was characterized by XRD (Bruker D2 Phaser). The phase composition was determined using a Partial or No Known Crystal Structure method,^[66] which was implemented in the Bruker TOPAS software. The Raman spectra were collected using a LabRAM HR 800 spectrometer with an excitation laser wavelength of 633 nm. Thermogravimetric analysis (TGA; TA Instruments Q500) was conducted under air with a heating rate of 5 °C min⁻¹. SEM (JEOL JCM-7000 NeoScope), TEM (JEOL F200), and energy-dispersive X-ray spectroscopy (EDS) were used to examine the morphologies, microstructures, and chemical compositions of the samples, respectively. XPS (Thermo Fisher Scientific ESCALAB 250Xi) was used to analyze the surface chemical states. Monochromatic Al K α radiation (1486.6 eV) was adopted as the X-ray source. The particle size distribution of various samples was estimated using a DLS (Otsuka ELSZ-2000) method, in which anhydrous ethanol was used to disperse the particles. Cyclic voltammetry (CV; BioLogic BCS-810) was performed in the range of 0.01–2.0 V versus Li/Li⁺ with a potential sweep rate of 0.1 mV s⁻¹. EIS analysis was conducted with a frequency range of 10⁶–10⁻² Hz and an AC amplitude of 10 mV. The charge–discharge properties, in terms of capacity, rate capability, and cycling stability, of various electrodes were evaluated

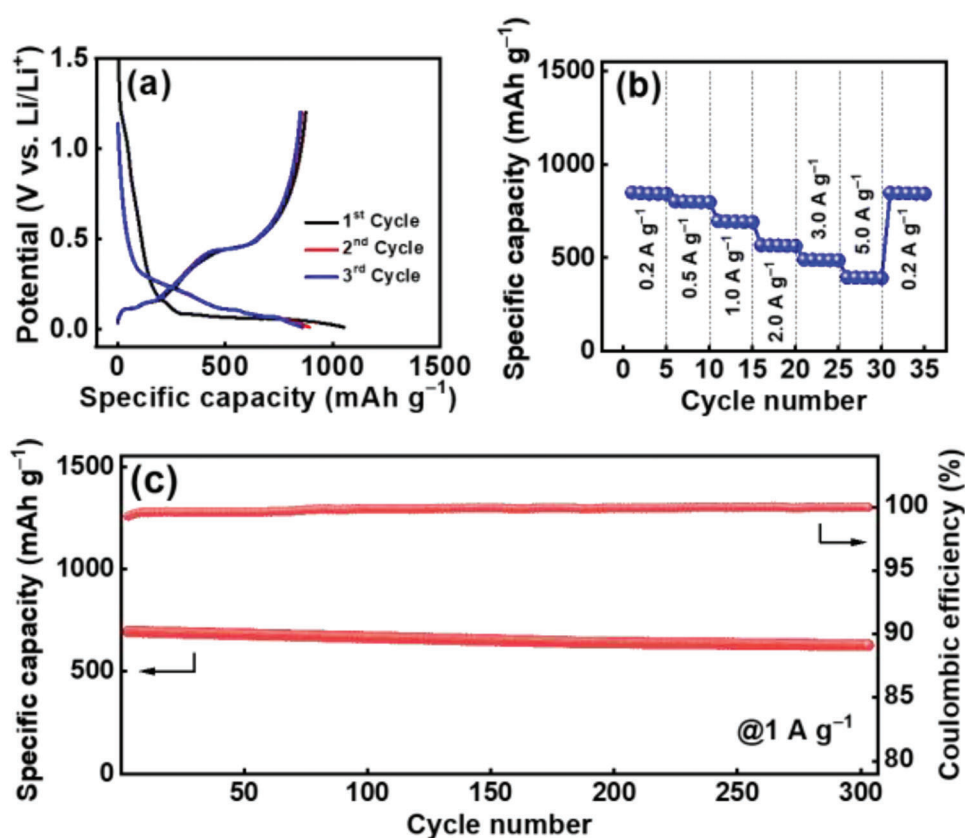


Figure 9. a) Initial three charge–discharge cycles, b) rate performance, and c) cycling stability of C- β -Si₃N₄/50%Si@AG electrode.

using a NEWARE CT-4000 battery tester at 25 °C. For the operando XRD analyses, the cells were subjected to synchrotron X-ray examination during charging/discharging at a rate of 0.5 A g⁻¹, which was performed at Beamline TPS-19A of the National Synchrotron Radiation Research Center in Taiwan.

Statistical Analysis: The DLS, CV, EIS, GITT, and charge–discharge measurements of various electrodes were repeated at least three times to ensure validity. The performance deviation was typically within $\approx 5\%$ and the reported data were the medians. All the XPS spectra were calibrated with the binding energy of C 1s peak at 284.7 eV. The data fitting was done using XPSPEAK 4.1 software. For XRD data, the background subtraction and phase identification were conducted using the EVA and TOPAS programs provided in Bruker software package. The Origin software was used for data analysis and processing.

Supporting Information

Supporting Information is available from the Wiley Online Library or from the author.

Acknowledgements

The financial support provided for this work by the National Science and Technology Council (NSTC) of Taiwan was gratefully appreciated.

Conflict of Interest

The authors declare no conflict of interest.

Data Availability Statement

The data that support the findings of this study are available from the corresponding author upon reasonable request.

Keywords

beta silicon nitride fraction, carbon coating, lithium nitride, operando X-ray diffraction, silicon nitride allotrope

Received: February 22, 2023

Revised: April 11, 2023

Published online:

- [1] J. B. Goodenough, K. S. Park, *J. Am. Chem. Soc.* **2013**, *135*, 1167.
- [2] P. Li, G. Q. Zhao, X. B. Zheng, X. Xu, C. H. Yao, W. P. Sun, S. X. Dou, *Energy Storage Mater.* **2018**, *15*, 422.
- [3] J. R. Szczech, S. Jin, *Energy Environ. Sci.* **2011**, *4*, 56.
- [4] M. Gu, Y. He, J. M. Zheng, C. M. Wang, *Nano Energy* **2015**, *17*, 366.
- [5] M. N. Obrovac, V. L. Chevrier, *Chem. Rev.* **2014**, *114*, 11444.
- [6] X. H. Liu, J. Y. Huang, *Energy Environ. Sci.* **2011**, *4*, 3844.
- [7] J. Lu, Z. W. Chen, F. Pan, Y. Cui, K. Amine, *Electrochem. Energy Rev.* **2018**, *1*, 35.
- [8] R. F. H. Hernandha, P. C. Rath, B. Umesh, J. Patra, C. Y. Huang, W. W. Wu, Q. F. Dong, J. Li, J. K. Chang, *Adv. Funct. Mater.* **2021**, *31*, 2104135.

- [9] N. Liu, Z. Lu, J. Zhao, M. T. McDowell, H. W. Lee, W. Zhao, Y. Cui, *Nat. Nanotechnol.* **2014**, *9*, 187.
- [10] M. Ashuri, Q. R. He, Y. Z. Liu, K. Zhang, S. Emani, M. S. Sawicki, J. S. Shamie, L. L. Shaw, *Electrochim. Acta* **2016**, *215*, 126.
- [11] H. Jia, X. Li, J. Song, X. Zhang, L. Luo, Y. He, B. Li, Y. Cai, S. Hu, X. Xiao, C. Wang, K. M. Rosso, R. Yi, R. Patel, J. G. Zhang, *Nat. Commun.* **2020**, *11*, 1474.
- [12] Y. Yang, W. Yuan, W. Q. Kang, Y. T. Ye, Q. Q. Pan, X. Q. Zhang, Y. Z. Ke, C. Wang, Z. Q. Qiu, Y. Tang, *Sustainable Energy Fuels* **2020**, *4*, 1577.
- [13] W. Wang, L. Gu, H. L. Qian, M. Zhao, X. Ding, X. S. Peng, J. Sha, Y. W. Wang, *J. Power Sources* **2016**, *307*, 410.
- [14] X. Y. Zhang, W. L. Song, Z. L. Liu, H. S. Chen, T. Li, Y. J. Wei, D. N. Fang, *J. Mater. Chem. A* **2017**, *5*, 12793.
- [15] L. Sun, Y. X. Liu, R. Shao, J. Wu, R. Y. Jiang, Z. Jin, *Energy Storage Mater.* **2022**, *46*, 482.
- [16] H. Kim, E. J. Lee, Y. K. Sun, *Mater. Today* **2014**, *17*, 285.
- [17] H. C. Song, H. X. Wang, Z. X. Lin, X. F. Jiang, L. W. Yu, J. Xu, Z. W. Yu, X. W. Zhang, Y. J. Liu, P. He, L. J. Pan, Y. Shi, H. S. Zhou, K. J. Chen, *Adv. Funct. Mater.* **2016**, *26*, 524.
- [18] Y. Chen, J. Qian, Y. Cao, H. Yang, X. Ai, *ACS Appl. Mater. Interfaces* **2012**, *4*, 3753.
- [19] P. X. Zhang, L. Huang, Y. L. Li, X. Z. Ren, L. B. Deng, Q. H. Yuan, *Electrochim. Acta* **2016**, *192*, 385.
- [20] K. M. Lee, Y. S. Lee, Y. W. Kim, Y. K. Sun, S. M. Lee, *J. Alloys Compd.* **2009**, *472*, 461.
- [21] S. Chae, M. Ko, S. Park, N. Kim, J. Ma, J. Cho, *Energy Environ. Sci.* **2016**, *9*, 1251.
- [22] H. I. Park, M. Sohn, J. H. Choi, C. Park, J. H. Kim, H. Kim, *Electrochim. Acta* **2016**, *210*, 301.
- [23] S. B. Son, S. C. Kim, C. S. Kang, T. A. Yersak, Y. C. Kim, C. G. Lee, S. H. Moon, J. S. Cho, J. T. Moon, K. H. Oh, S. H. Lee, *Adv. Energy Mater.* **2012**, *2*, 1226.
- [24] Y. Domi, H. Usui, R. Takaishi, H. Sakaguchi, *ChemElectroChem* **2019**, *6*, 581.
- [25] R. A. Vila, W. Huang, Y. Cui, *Cell Rep. Phys. Sci.* **2020**, *1*, 100188.
- [26] C. Zhan, T. P. Wu, J. Lu, K. Amine, *Energy Environ. Sci.* **2018**, *11*, 243.
- [27] J. S. Edge, S. O'Kane, R. Prosser, N. D. Kirkaldy, A. N. Patel, A. Hales, A. Ghosh, W. Ai, J. Chen, J. Yang, S. Li, M. C. Pang, L. Bravo Diaz, A. Tomaszewska, M. W. Marzook, K. N. Radhakrishnan, H. Wang, Y. Patel, B. Wu, G. J. Offer, *Phys. Chem. Chem. Phys.* **2021**, *23*, 8200.
- [28] O. C. Harris, Y. X. Lin, Y. Qi, K. Leung, M. H. Tang, *J. Electrochem. Soc.* **2020**, *167*, 013502.
- [29] X. N. Zhang, G. L. Pan, G. R. Li, J. Q. Qu, X. P. Gao, *Solid State Ionics* **2007**, *178*, 1107.
- [30] S. J. Kim, M. C. Kim, S. B. Han, G. H. Lee, H. S. Choe, D. H. Kwak, S. Y. Choi, B. G. Son, M. S. Shin, K. W. Park, *Nano Energy* **2016**, *27*, 545.
- [31] Z. X. Xiao, C. Lei, C. H. Yu, X. Chen, Z. X. Zhu, H. R. Jiang, F. Wei, *Energy Storage Mater.* **2020**, *24*, 565.
- [32] X. L. Qu, X. Zhang, Y. J. Wu, J. J. Hu, M. X. Gao, H. G. Pan, Y. F. Liu, *J. Power Sources* **2019**, *443*, 227265.
- [33] F. L. Riley, *J. Am. Ceram. Soc.* **2000**, *83*, 245.
- [34] J. F. Yang, T. Ohji, S. Kanzaki, A. Diaz, S. Hampshire, *J. Am. Ceram. Soc.* **2002**, *85*, 1512.
- [35] E. T. Turkdogan, P. M. Bills, V. A. Tippet, *J. Appl. Chem.* **1958**, *8*, 296.
- [36] G. Ziegler, J. Heinrich, G. Wotting, *J. Mater. Sci.* **1987**, *22*, 3041.
- [37] R. Grün, *Acta Crystallogr., Sect. B: Struct. Sci., Cryst. Eng. Mater.* **1979**, *35*, 800.
- [38] R. J. Lad, in *Physical Structure*, (Ed: W. N. Unertl), Elsevier Science B. V, North-Holland **1996**, Vol. 1, Ch. 5.
- [39] A. C. Ferrari, J. Robertson, *Phys. Rev. B* **2000**, *61*, 14095.
- [40] H. J. Scheibe, D. Drescher, P. Alers, *Fresenius' J. Anal. Chem.* **1995**, *353*, 695.
- [41] A. E. Kaloyeros, F. A. Jov \acute{e} , J. Goff, B. Arkles, *ECS J. Solid State Sci. Technol.* **2017**, *6*, P691.
- [42] K. Kijima, S. Shirasaki, *J. Chem. Phys.* **1976**, *65*, 2668.
- [43] J. D. Xie, H. Y. Li, B. Umesh, T. C. Lee, J. K. Chang, Y. A. Gandomi, *Electrochim. Acta* **2018**, *292*, 951.
- [44] J. Patra, P. C. Rath, C. Li, H. M. Kao, F. M. Wang, J. Li, J. K. Chang, *ChemSusChem* **2018**, *11*, 3923.
- [45] P. Lengsfeld, S. Brehme, K. Brendel, C. Genzel, N. H. Nickel, *Phys. Status Solidi B* **2003**, *235*, 170.
- [46] D. C. Lin, Z. D. Lu, P. C. Hsu, H. R. Lee, N. Liu, J. Zhao, H. T. Wang, C. Liu, Y. Cui, *Energy Environ. Sci.* **2015**, *8*, 2371.
- [47] G. Ge, G. Li, X. Wang, X. Chen, L. Fu, X. Liu, E. Mao, J. Liu, X. Yang, C. Qian, Y. Sun, *Nano Lett.* **2021**, *21*, 3127.
- [48] C. Zhang, F. Wang, J. Han, S. Bai, J. Tan, J. Liu, F. Li, *Small Struct.* **2021**, *2*, 2100009.
- [49] Y. Surace, D. Leanza, M. Mirolo, Ł. Kondracki, C. A. F. Vaz, M. El Kazzi, P. Novák, S. Trabesinger, *Energy Storage Mater.* **2022**, *44*, 156.
- [50] I. A. Profatilova, C. Stock, A. Schmitz, S. Passerini, M. Winter, *J. Power Sources* **2013**, *222*, 140.
- [51] M. N. Obrovac, L. J. Krause, *J. Electrochem. Soc.* **2007**, *154*, A103.
- [52] Q. Wang, M. Zhu, G. Chen, N. Dudko, Y. Li, H. Liu, L. Shi, G. Wu, D. Zhang, *Adv. Mater.* **2022**, *34*, 2109658.
- [53] C. H. Jung, K. H. Kim, S. H. Hong, *ACS Appl. Mater. Interfaces* **2019**, *11*, 26753.
- [54] K. Pan, F. Zou, M. Canova, Y. Zhu, J. H. Kim, *J. Power Sources* **2019**, *413*, 20.
- [55] B. Umesh, P. C. Rath, J. Patra, R. F. H. Hernandha, S. B. Majumder, X. Gao, D. Bresser, S. Passerini, H. Z. Lai, T. L. Chang, J. K. Chang, *Chem. Eng. J.* **2022**, *430*, 132693.
- [56] J. H. Yang, R. C. de Guzman, S. O. Salley, K. Y. S. Ng, B. H. Chen, M. M. C. Cheng, *J. Power Sources* **2014**, *269*, 520.
- [57] S. X. Mei, S. G. Guo, B. Xiang, J. G. Deng, J. J. Fu, X. M. Zhang, Y. Zheng, B. Gao, P. K. Chu, K. F. Huo, *J. Energy Chem.* **2022**, *69*, 616.
- [58] Y. M. Sun, Y. B. Li, J. Sun, Y. Z. Li, A. Pei, Y. Cui, *Energy Storage Mater.* **2017**, *6*, 119.
- [59] S. Chae, S. Park, K. Ahn, G. Nam, T. Lee, J. Sung, N. Kim, J. Cho, *Energy Environ. Sci.* **2020**, *13*, 1212.
- [60] U. v. Alpen, *J. Solid State Chem.* **1979**, *29*, 379.
- [61] H. P. Klug, L. E. Alexander, *X-Ray Diffraction Procedures: For Polycrystalline and Amorphous Materials*, John Wiley & Sons, Inc., New York, USA **1974**.
- [62] Y. Domi, H. Usui, K. Sugimoto, H. Sakaguchi, *Energy Technol.* **2019**, *7*, 1800946.
- [63] D. S. M. Iaboni, M. N. Obrovac, *J. Electrochem. Soc.* **2015**, *163*, A255.
- [64] Sutarsis, J. Patra, C. Y. Su, J. Li, D. Bresser, S. Passerini, J. K. Chang, *ACS Appl. Mater. Interfaces* **2020**, *12*, 32797.
- [65] B. Umesh, P. C. Rath, R. F. H. Hernandha, J. Y. Lin, S. B. Majumder, Q. F. Dong, J. K. Chang, *ACS Sustainable Chem. Eng.* **2020**, *8*, 16252.
- [66] N. V. Y. Scarlett, I. C. Madsen, *Powder Diffr.* **2006**, *21*, 278.

Supporting Information

for *Adv. Sci.*, DOI 10.1002/adv.202301218

N-Containing Carbon-Coated β -Si₃N₄ Enhances Si Anodes for High-Performance Li-Ion Batteries

*Rahmandhika Firdauzha Hary Hernandha, Bharath Umesh, Purna Chandra Rath, Le Thi Thu Trang, Ju-Chao Wei, Yu-Chun Chuang, Ju Li and Jeng-Kuei Chang**

Supporting Information

N-containing carbon-coated β -Si₃N₄ enhances Si anodes for high-performance Li-ion batteries

*Rahmandhika Firdauzha Hary Hernandha, Bharath Umesh, Purna Chandra Rath, Le Thi Thu Trang, Ju-Chao Wei, Yu-Chun Chuang, Ju Li, Jeng-Kuei Chang**

Table S1. Electronic conductivity data of various samples.

Samples	Electronic conductivity ($\times 10^{-1}$ S cm ⁻¹)
C- α -Si ₃ N ₄	1.02
C- β -Si ₃ N ₄	1.07
C- β -Si ₃ N ₄ /25%Si	1.51
C- β -Si ₃ N ₄ /50%Si	1.92
C- β -Si ₃ N ₄ /75%Si	2.35
C-Si	2.76

Table S2. Reversible specific capacities of α -Si₃N₄, β -Si₃N₄, C- α -Si₃N₄, and C- β -Si₃N₄ electrodes measured at various specific currents.

Current rate (A g ⁻¹)	α -Si ₃ N ₄ (mAh g ⁻¹)	β -Si ₃ N ₄ (mAh g ⁻¹)	C- α -Si ₃ N ₄ (mAh g ⁻¹)	C- β -Si ₃ N ₄ (mAh g ⁻¹)
0.05	80	91	109	118
0.1	71	86	100	106
0.3	58	67	84	92
0.5	51	61	76	83
1	42	52	64	73
2	31	42	52	62
High rate retention*	39%	46%	48%	53%

* a comparison between reversible capacities at 2 and 0.05 A g⁻¹.

Table S3. Tap densities of various samples.

Samples	Tap density (g cm ⁻³)
C- β -Si ₃ N ₄	0.887
C- β -Si ₃ N ₄ /25%Si	0.819
C- β -Si ₃ N ₄ /50%Si	0.802
C- β -Si ₃ N ₄ /75%Si	0.797
C-Si	0.572

Table S4. Expected capacities of various C- β -Si₃N₄/Si composite anodes calculated from linear combination of measured capacities of C- β -Si₃N₄ and C-Si electrodes. Synergistic effects are shown.

Current rate (A g ⁻¹)	C- β -Si ₃ N ₄ (mAh g ⁻¹)	C- β -Si ₃ N ₄ /25%Si (mAh g ⁻¹)			C- β -Si ₃ N ₄ /50%Si (mAh g ⁻¹)			C- β -Si ₃ N ₄ /75%Si (mAh g ⁻¹)			C-Si (mAh g ⁻¹)
		Actual capacity (A)	Expected capacity (E)	$\frac{(A)}{(E)}$	Actual capacity (A)	Expected capacity (E)	$\frac{(A)}{(E)}$	Actual capacity (A)	Expected capacity (E)	$\frac{(A)}{(E)}$	
0.2	100	583	530	1.10	1068	960	1.11	1390	1390	1.00	1820
0.5	83	525	460	1.14	1000	837	1.19	1218	1214	1.00	1591
1	73	476	382	1.24	935	692	1.35	1124	1002	1.12	1311
2	62	424	297	1.43	769	532	1.45	930	766	1.21	1001
3	55	365	232	1.57	670	410	1.63	728	588	1.24	765
5	46	250	144	1.74	488	242	2.02	452	339	1.33	437

Table S5. Performance comparison of various Si-based composite anodes reported in the literature.

No.	Material	Synthesis method	Initial reversible capacity (mAh g ⁻¹)	Initial Coulombic efficiency (%)	Capacity retention (%) / number of cycles / current rate (A g ⁻¹)	References
1	α -Si ₃ N ₄	Ball milling (reduce size with time dependent)	83	~40	N/A	[1]
2	α -Si ₃ N ₄ w + 30 % Si composites	Ball milling	>800	~40	~27 / 50 / 0.08	[2]
3	a-Si ₃ N ₄ p + 30 % Si composites	Ball milling	~1000	~50	~47 / 50 / 0.08	[2]
4	Si _{3-x} M _x N ₄ (M=Fe)	Manual mix of α -Si ₃ N ₄ +Fe and pelletized	470.6	50.5	45.4 / 50 / 0.1 C	[3]
5	Ti ₂₈ Si ₇₂ melt-spun powders	Ball milling of pre-alloyed melt-spun Ti-Si	~260	~67	~85 / ~47 / 2 x 10 ⁻⁴ A cm ⁻²	[4]
6	Binder-free a-SiN/BCNT	Hot filament CVD & sputtering	607	N/A	62 / 10 / 2 x 10 ⁻⁴ A cm ⁻²	[5]
7	Cu-coated Si (empowered by CuO, Cu ₃ Si, SiO, and SiO ₂) nanowires	CVD and magnetron sputtering	2679	90.3	59 / 50 / 0.5 C	[6]
8	Si-Ti-Ni ternary nanoalloy	Single-roller melt-spinning technique	1158	87.7	~82 / 50 / 8.8 x 10 ⁻⁴ A cm ⁻²	[7]
9	FeSi ₂ /Si@C Nanocomposite	Two-step ball-milling process	942	72	93 / 200 / 0.1	[8]
10	a-SiN _{0.92}	Pulsed Laser Deposition	1800	~75	72.2 / 100 / 0.2 C	[9]
11	a-SiN _x /graphene	CVD, dispersion, and heat treatment	>3000	70	45.2 / 200 / 0.5	[10]
12	Hollow silicon nanosphere	Sol-gel method, magnesiothermic and hydrogen reductions, and acid etching	1610	72.2	~80 / 120 / 1	[11]

13	C-coated Si nanotube	Two-step CVD and selective thermal reduction etching	~3823	87	~81 / 80 (20 th –100 th) / 1 C	[12]
14	Si@ α -Si ₃ N ₄ /CNF	Mixing & electrospinning	613	61.4	55.5 / 2000 / 10	[13]
15	N1-Si/CMAAs (a-SiN _{0.73})	Two-step DC sputtering on Cu Micro-cone arrays (CMAAs)	2789	80	40 / 200 / 0.2 C	[14]
16	Si/TiFeSi ₂ Nanocomposite	Melt spinning fabrication method and ball-milling	~1000	~80	~90 / 100 / 0.2	[15]
17	Si–Cu alloy (mixture) nanotubes	Vapor-solid oxidation mechanism, plasma enhanced CVD, and heat treatment	~1700	42	76.2 / 100 / 3.2	[16]
18	Si/Ni ₃ Si-Encapsulated CNF Composites	One-pot electrospinning method	~855	72.5	N/A (capacity is increasing during cycling)	[17]
19	Micron-sized Fe–Cu–Si ternary composite	CVD, spray-drying, and elevated temperature reduction process	1287	91.4	90 / 50 / 0.65	[18]
20	a-SiN _x -H	Plasma Enhanced CVD	32	69.1	N/A (capacity was increasing until 200 th and lowering until 350 th cycle)	[19]
21	Si@Si ₃ N ₄ @C	Two-step gas–solid reaction	3093.8	91.5	81.3 / 200 / 0.5	[20]
22	SiN _{0.7} nanoparticles	Gas-phase synthesis	1212	~55	82 / 300 / 0.5 C	[21]
23	p-Si@SiN	Direct nitriding hydrogenated porous Si	2584	81	84 / 200 / 0.5	[22]
24	C-β-Si₃N₄/50%Si	Ball milling &	1068	78	75 / 300 / 1	This work
25	C-β-Si₃N₄/50%Si@AG	wet chemical coating	849	83	90 / 300 / 1	This work

References

- [1] M. Martín-Gil, M. E. Rabanal, A. Várez, A. Kuhn, F. García-Alvarado, *Mater. Lett.* **2003**, *57*, 3063.
- [2] X. N. Zhang, G. L. Pan, G. R. Li, J. Q. Qu, X. P. Gao, *Solid State Ion.* **2007**, *178*, 1107.
- [3] N. Kalaiselvi, *Int. J. Electrochem. Sci.* **2007**, *2*, 478.
- [4] K. M. Lee, Y. S. Lee, Y. W. Kim, Y. K. Sun, S. M. Lee, *J. Alloys Compd.* **2009**, *472*, 461.
- [5] S. L. Katar, D. Hernandez, A. B. Labiosa, E. Mosquera-Vargas, L. Fonseca, B. Weiner, G. Morell, *Electrochim. Acta* **2010**, *55*, 2269.
- [6] H. Chen, Y. Xiao, L. Wang, Y. Yang, *J. Power Sources* **2011**, *196*, 6657.
- [7] S. B. Son, S. C. Kim, C. S. Kang, T. A. Yersak, Y. C. Kim, C. G. Lee, S. H. Moon, J. S. Cho, J. T. Moon, K. H. Oh, S. H. Lee, *Adv. Energy Mater.* **2012**, *2*, 1226.
- [8] Y. Chen, J. Qian, Y. Cao, H. Yang, X. Ai, *ACS Appl. Mater. Interfaces* **2012**, *4*, 3753.
- [9] N. Suzuki, R. B. Cervera, T. Ohnishi, K. Takada, *J. Power Sources* **2013**, *231*, 186.
- [10] R. C. de Guzman, J. Yang, M. M. C. Cheng, S. O. Salley, K. Y. S. Ng, *J. Mater. Chem. A* **2014**, *2*, 14577.
- [11] M. Ashuri, Q. R. He, Y. Z. Liu, K. Zhang, S. Emani, M. S. Sawicki, J. S. Shamie, L. L. Shaw, *Electrochim. Acta* **2016**, *215*, 126.
- [12] W. Wang, L. Gu, H. L. Qian, M. Zhao, X. Ding, X. S. Peng, J. Sha, Y. W. Wang, *J. Power Sources* **2016**, *307*, 410.
- [13] S. J. Kim, M. C. Kim, S. B. Han, G. H. Lee, H. S. Choe, D. H. Kwak, S. Y. Choi, B. G. Son, M. S. Shin, K. W. Park, *Nano Energy* **2016**, *27*, 545.
- [14] C. Y. Wu, C. C. Chang, J. G. Duh, *J. Power Sources* **2016**, *325*, 64.

- [15] H. I. Park, M. Sohn, J. H. Choi, C. Park, J. H. Kim, H. Kim, *Electrochim. Acta* **2016**, *210*, 301.
- [16] H. C. Song, H. X. Wang, Z. X. Lin, X. F. Jiang, L. W. Yu, J. Xu, Z. W. Yu, X. W. Zhang, Y. J. Liu, P. He, L. J. Pan, Y. Shi, H. S. Zhou, K. J. Chen, *Adv. Funct. Mater.* **2016**, *26*, 524.
- [17] P. X. Zhang, L. Huang, Y. L. Li, X. Z. Ren, L. B. Deng, Q. H. Yuan, *Electrochim. Acta* **2016**, *192*, 385.
- [18] S. Chae, M. Ko, S. Park, N. Kim, J. Ma, J. Cho, *Energy Environ. Sci.* **2016**, *9*, 1251.
- [19] X. D. Huang, X. F. Gan, F. Zhang, Q. A. Huang, J. Z. Yang, *Electrochim. Acta* **2018**, *268*, 241.
- [20] Z. X. Xiao, C. Lei, C. H. Yu, X. Chen, Z. X. Zhu, H. R. Jiang, F. Wei, *Energy Storage Mater.* **2020**, *24*, 565.
- [21] S. O. Kilian, H. Wiggers, *Part. Part. Syst. Character.* **2021**, *38*, 2100007.
- [22] S. X. Mei, S. G. Guo, B. Xiang, J. G. Deng, J. J. Fu, X. M. Zhang, Y. Zheng, B. Gao, P. K. Chu, K. F. Huo, *J. Energy Chem.* **2022**, *69*, 616.

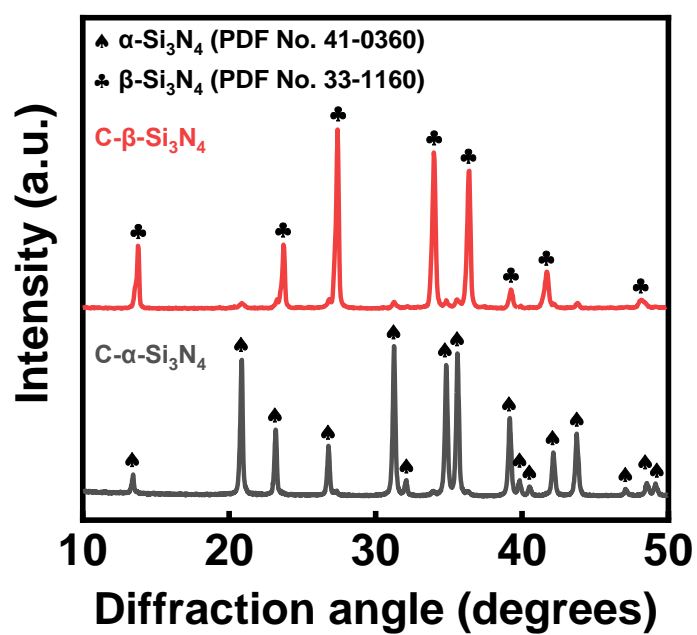


Figure S1. XRD patterns of C- α - Si_3N_4 and C- β - Si_3N_4 .

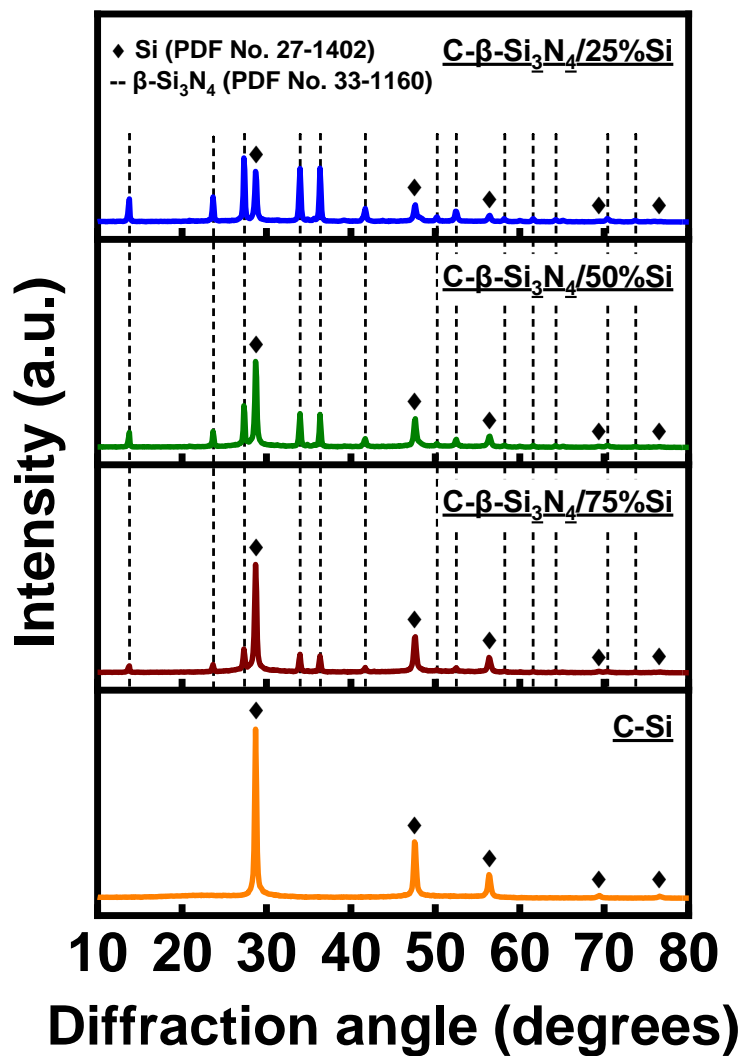


Figure S2. XRD patterns of C- β - Si_3N_4 /25%Si, C- β - Si_3N_4 /50%Si, C- β - Si_3N_4 /75%Si, and C-Si samples.

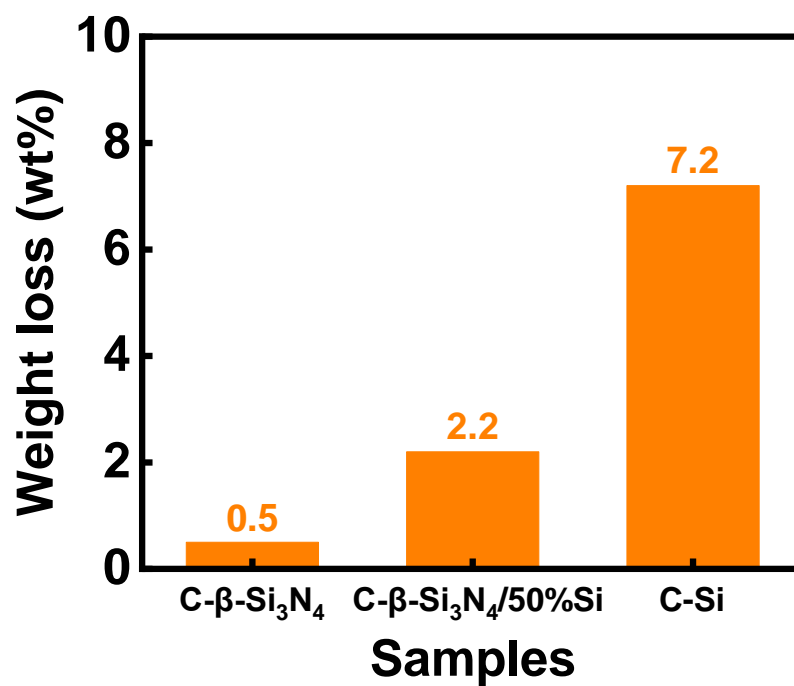


Figure S3. Weight loss data for C-β-Si₃N₄, C-β-Si₃N₄/50%Si, and C-Si after immersion in 25 mM HF aqueous solution at 25 °C for 1 h.

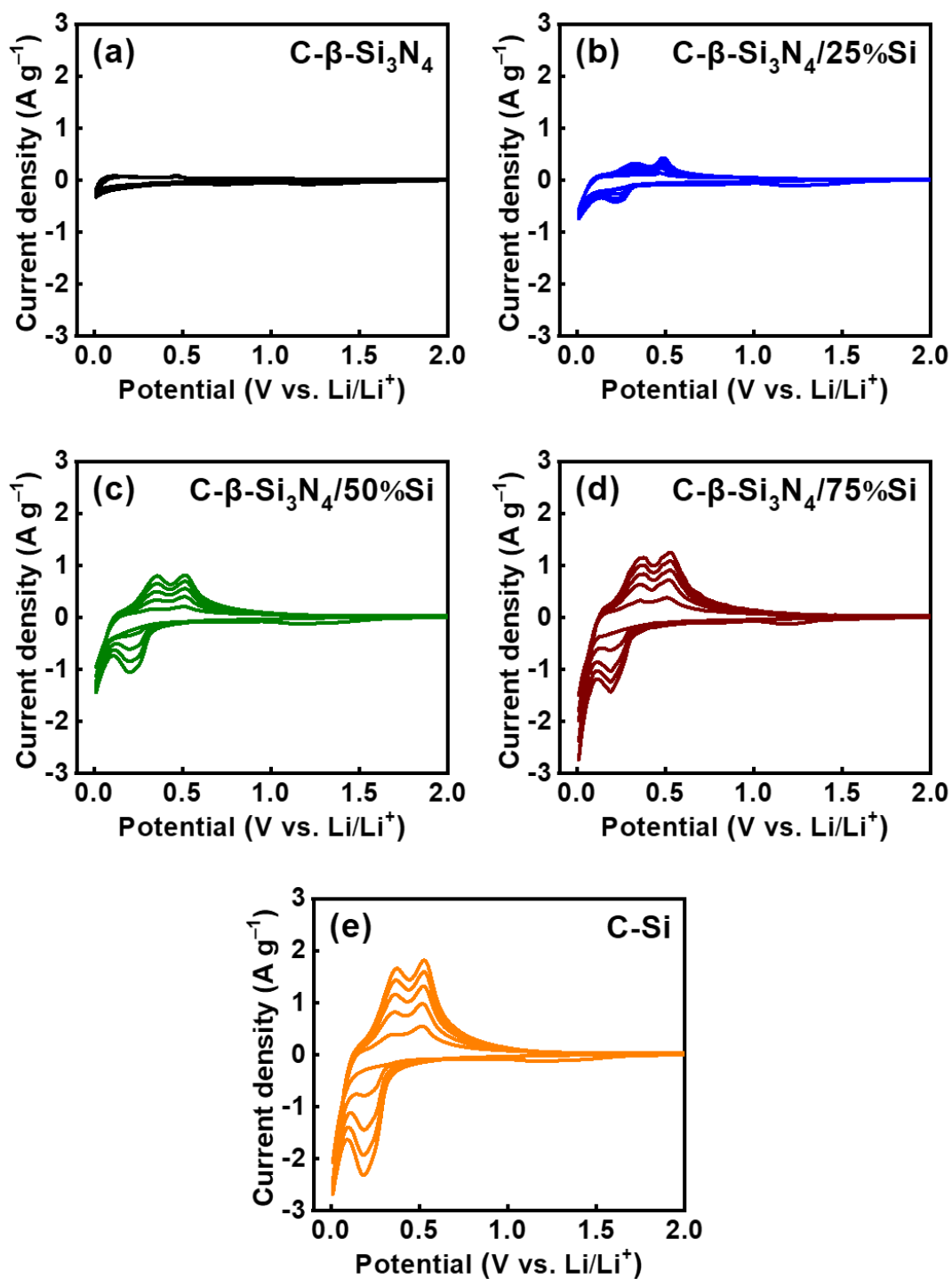


Figure S4. CV curves of (a) C-β-Si₃N₄, (b) C-β-Si₃N₄/25%Si, (c) C-β-Si₃N₄/50%Si, (d) C-β-Si₃N₄/75%Si, and (e) C-Si electrodes recorded with potential scan rate of 0.1 mV s⁻¹ for 5 cycles.

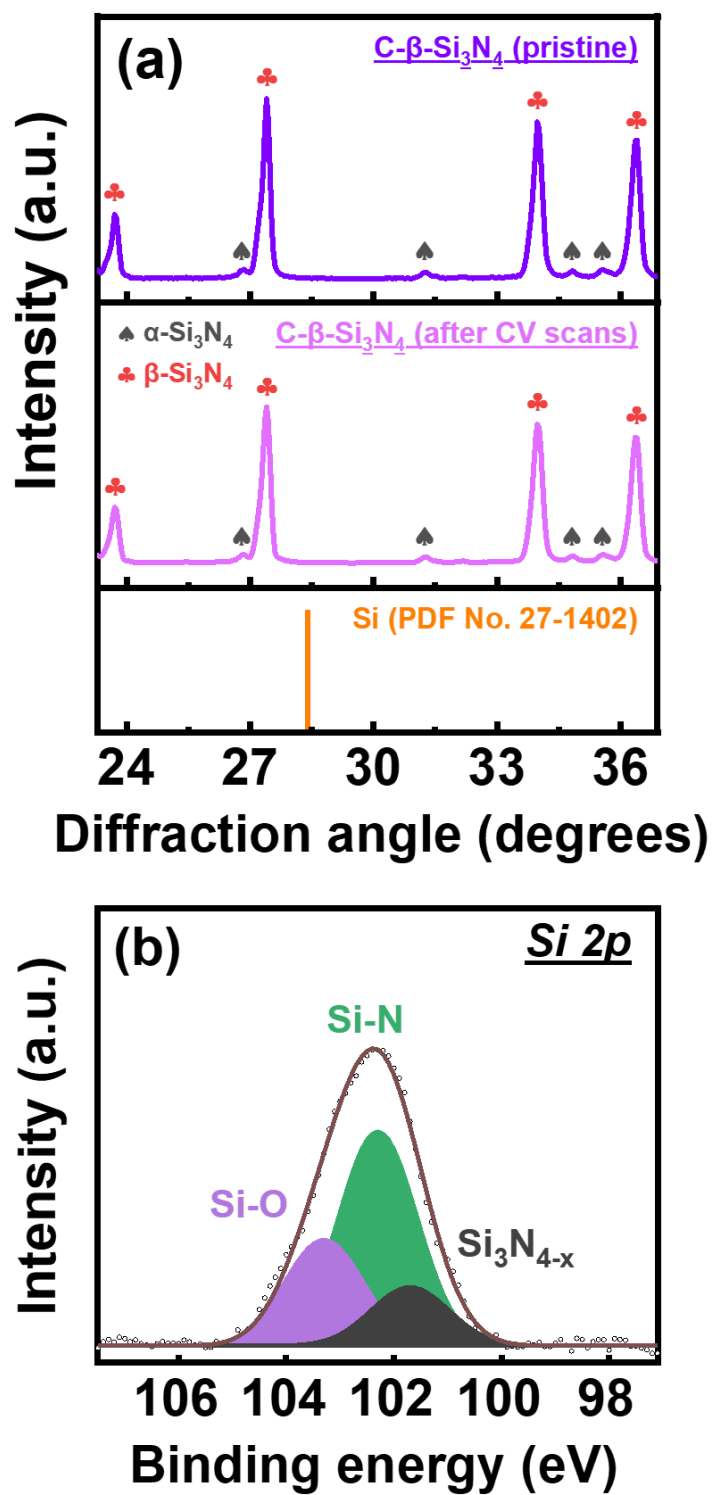


Figure S5. (a) XRD data of C-β-Si₃N₄ electrode before and after CV scans. (b) XPS Si 2p spectrum of C-β-Si₃N₄ electrode after CV scans.

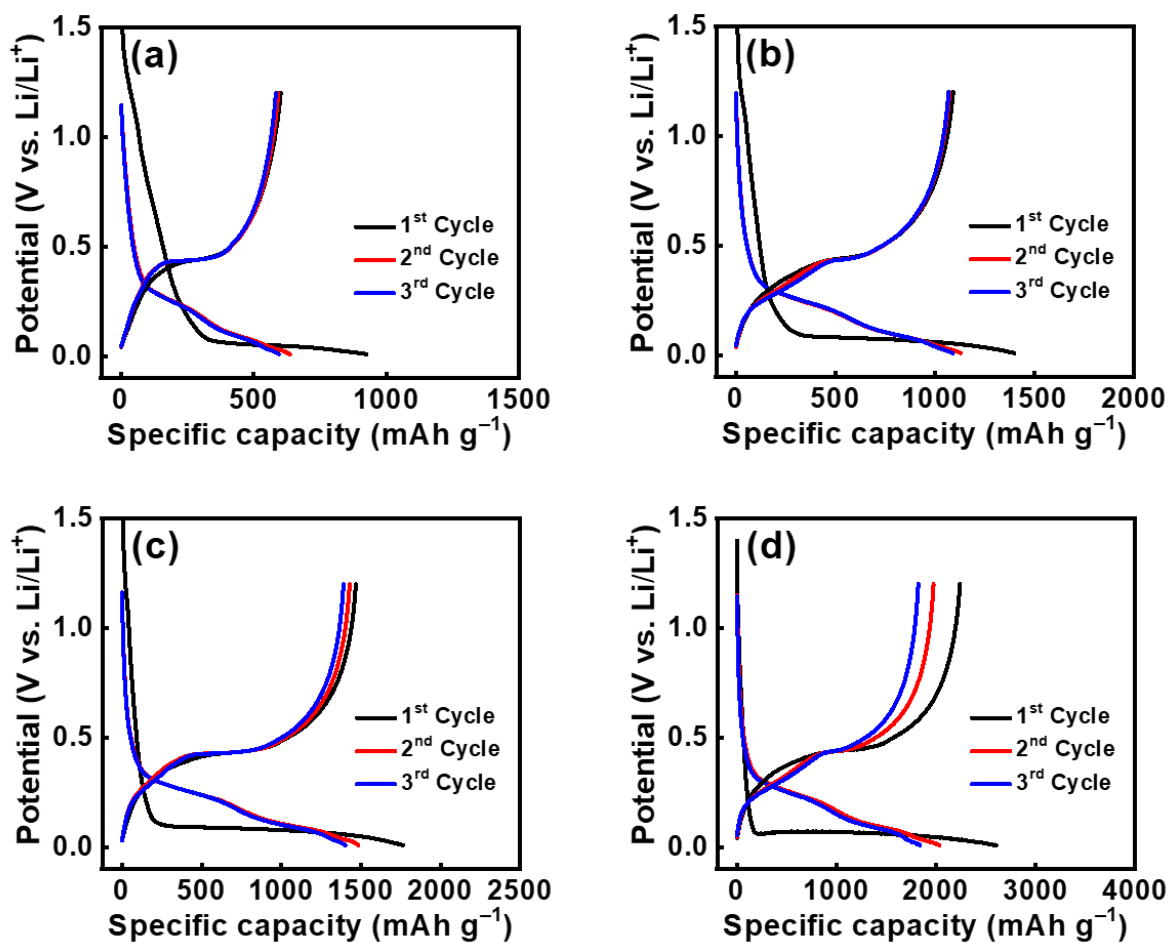


Figure S6. Initial three charge–discharge cycles of (a) C- β -Si₃N₄/25%Si, (b) C- β -Si₃N₄/50%Si, (c) C- β -Si₃N₄/75%Si, and (d) C-Si electrodes measured at 0.2 A g⁻¹.

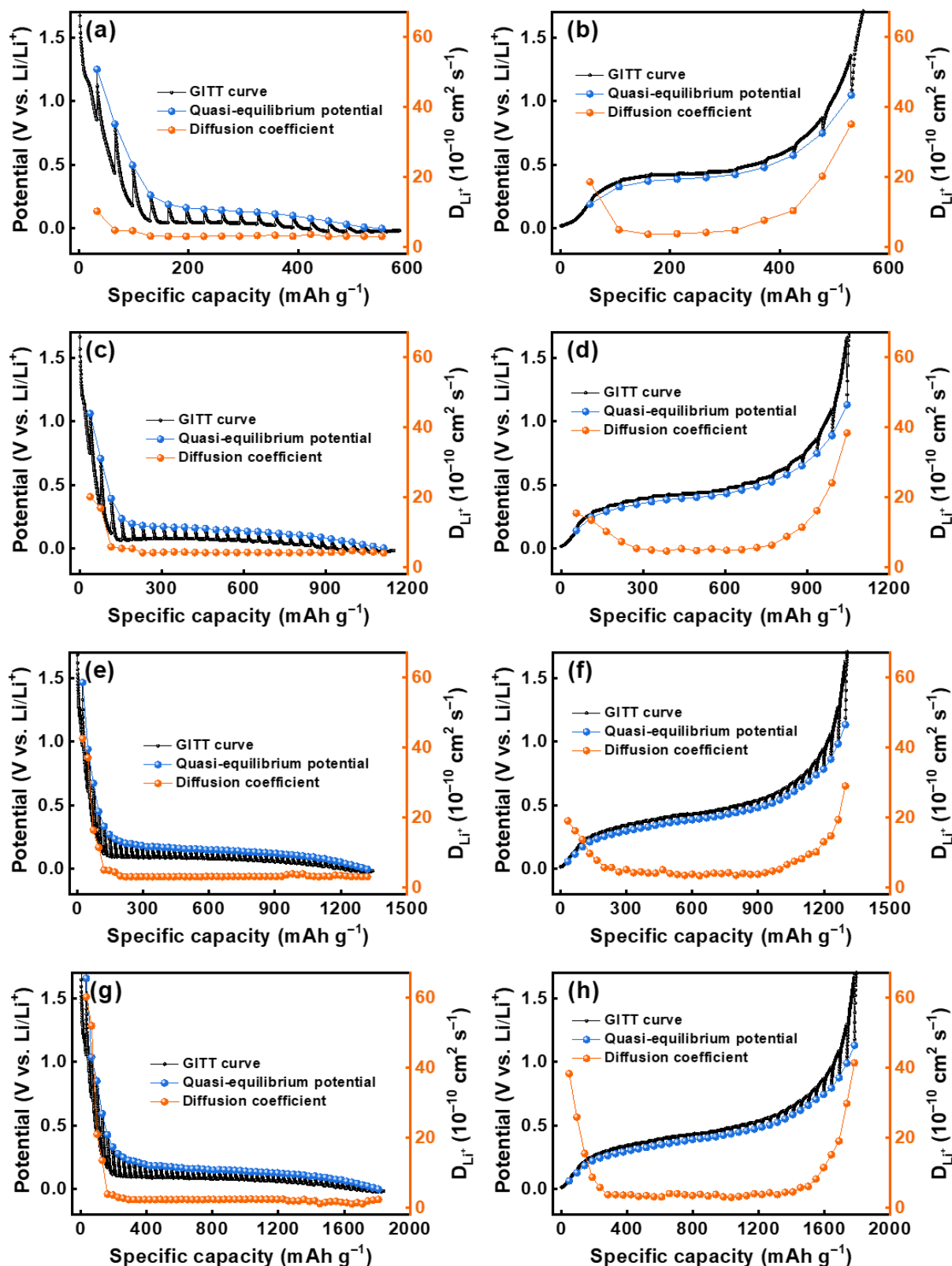


Figure S7. GITT measurements of (a, b) C- β -Si₃N₄/25%Si, (c, d) C- β -Si₃N₄/50%Si, (e, f) C- β -Si₃N₄/75%Si, and (g, h) C-Si electrodes during lithiation and delithiation processes.

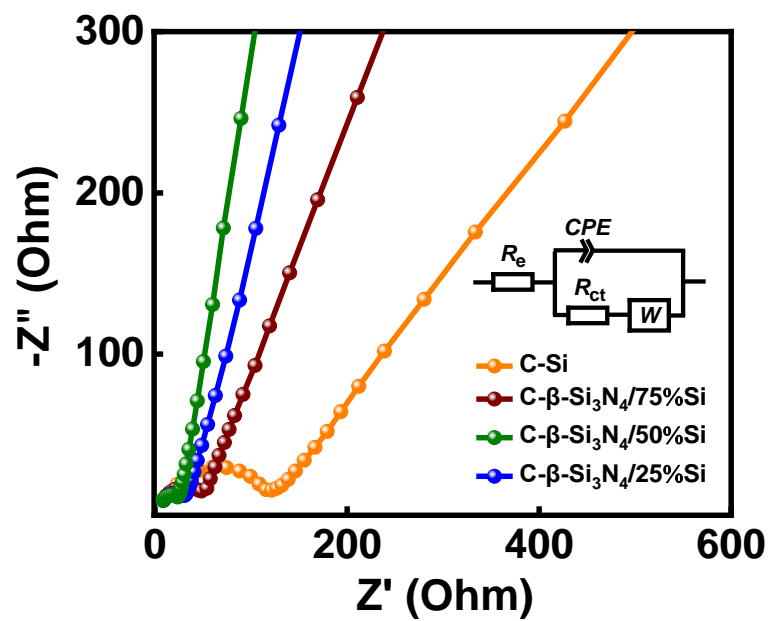


Figure S8. EIS data of various electrodes acquired after 300 charge–discharge cycles.

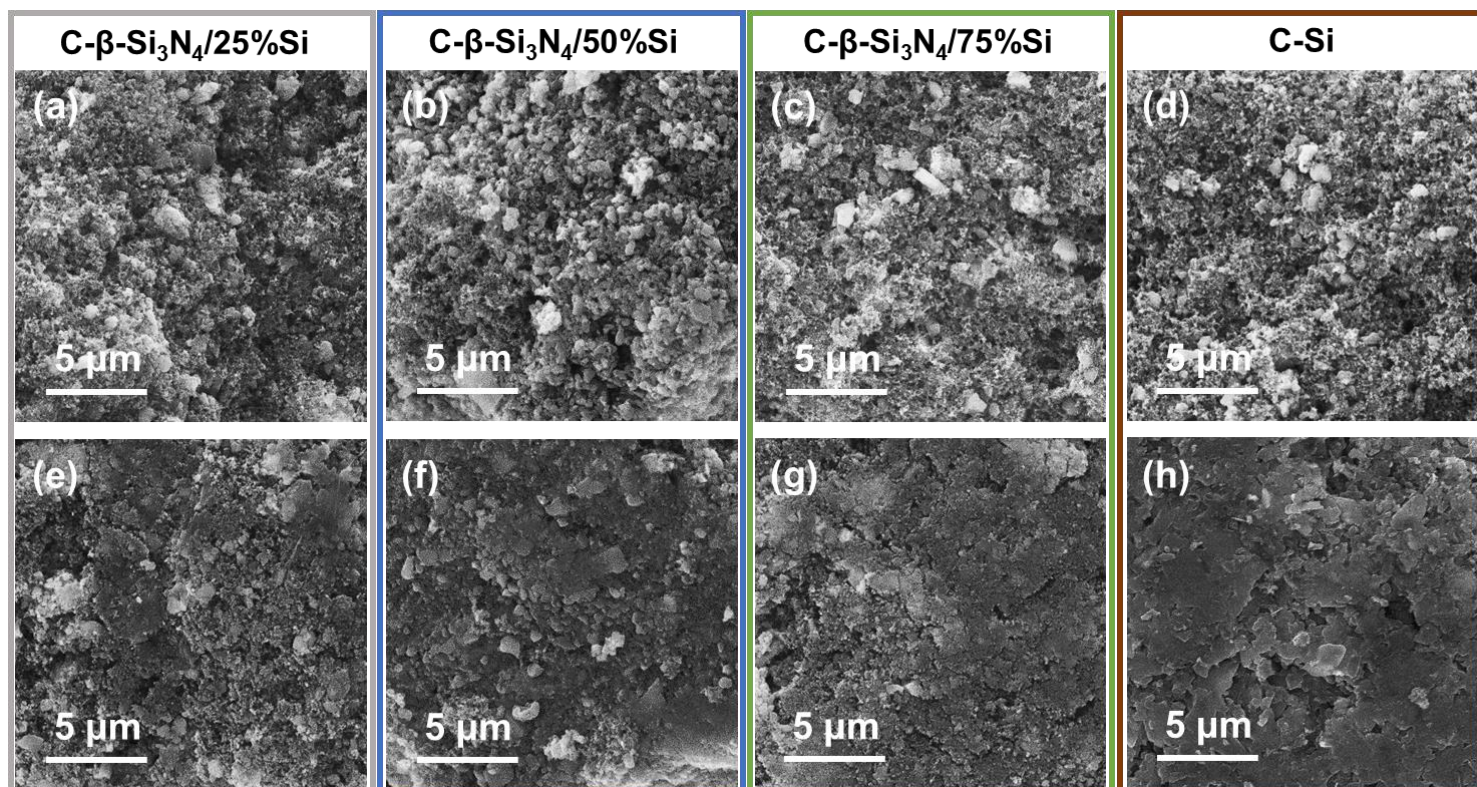


Figure S9. SEM images of C-β-Si₃N₄/25%Si, C-β-Si₃N₄/50%Si, C-β-Si₃N₄/75%Si, and C-Si electrodes (a–d) before and (e–h) after 300 charge–discharge cycles.

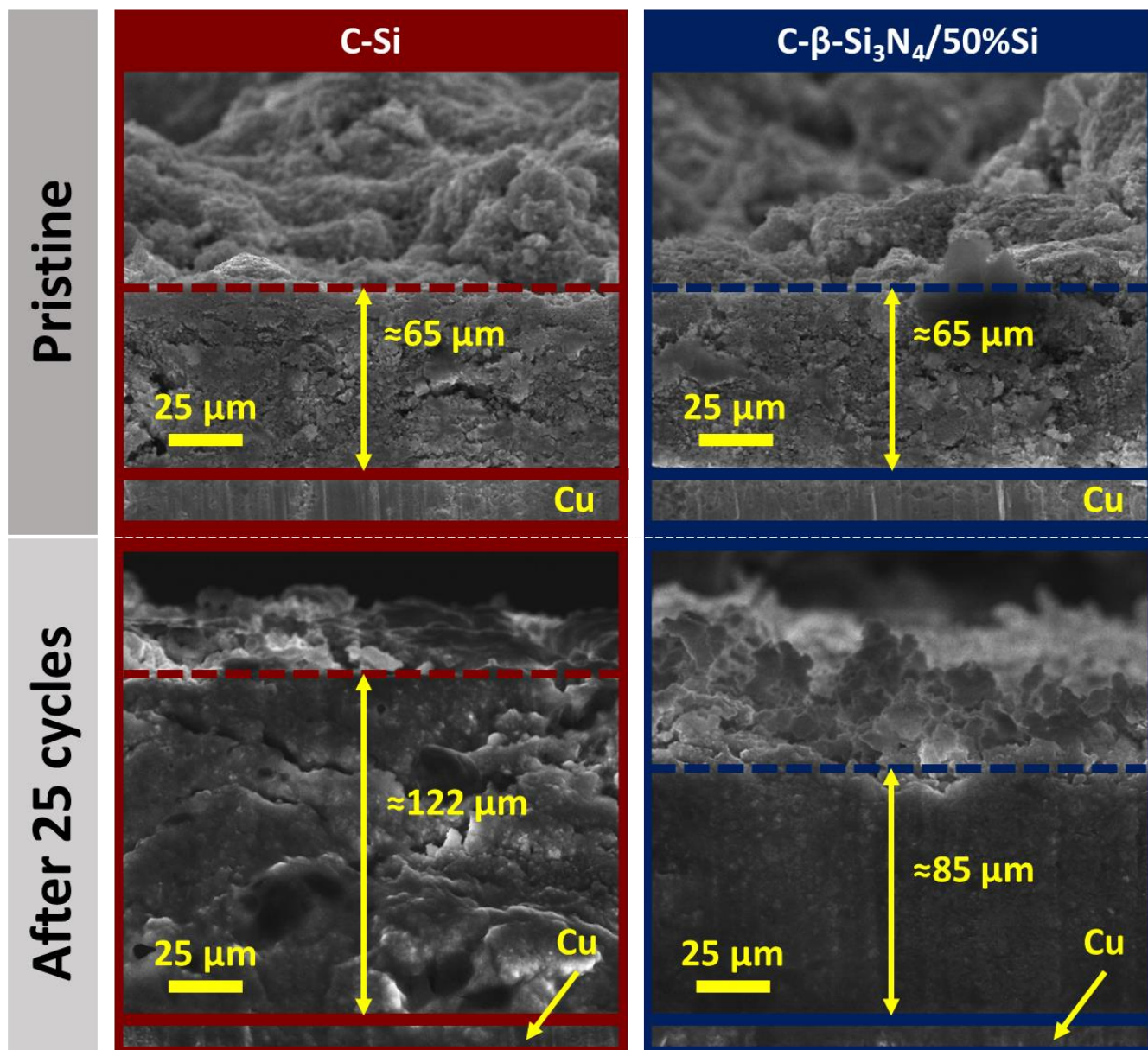


Figure S10. Cross-section SEM images of C-Si and C-β-Si₃N₄/50%Si electrodes before and after 25 charge–discharge cycles.

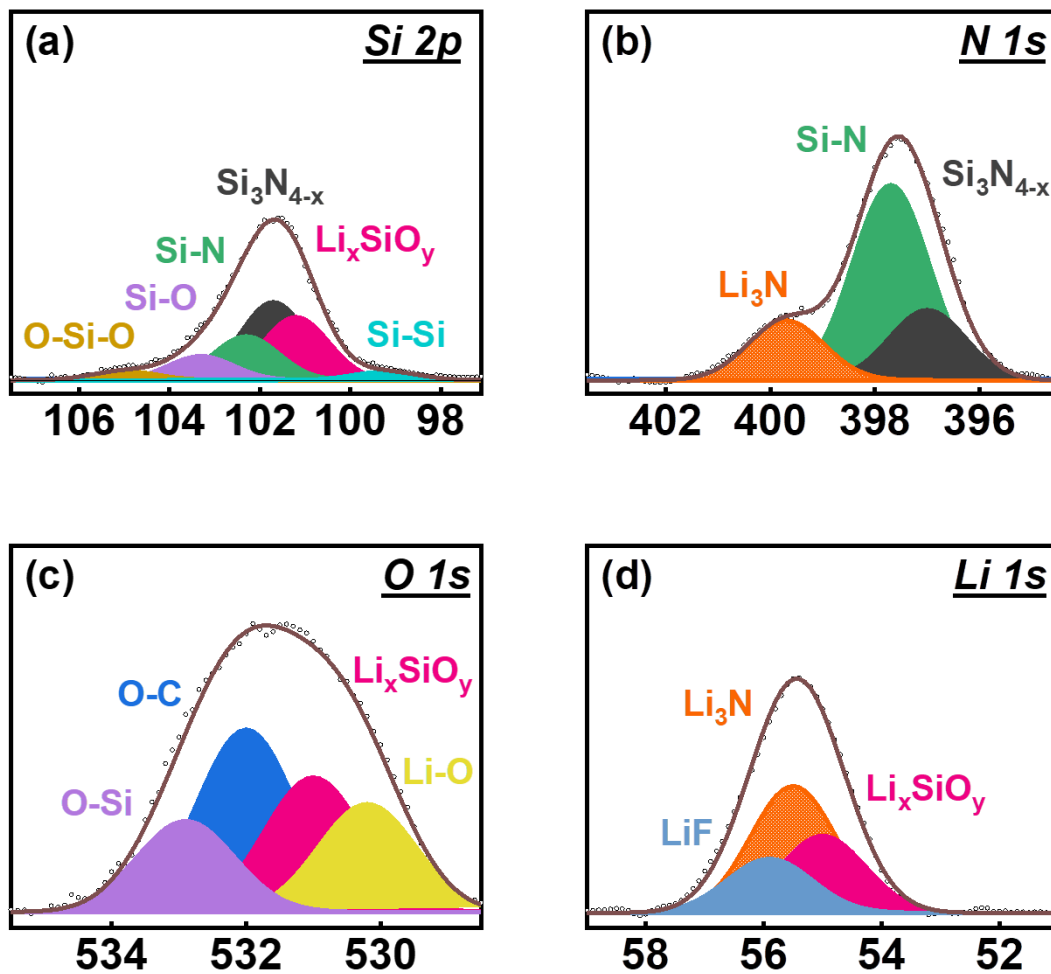


Figure S11. XPS (a) Si 2p, (b) N 1s, (c) O 1s, and (d) Li 1s spectra of C- β - $\text{Si}_3\text{N}_4/50\%\text{Si}$ electrode after 300 charge-discharge cycles.

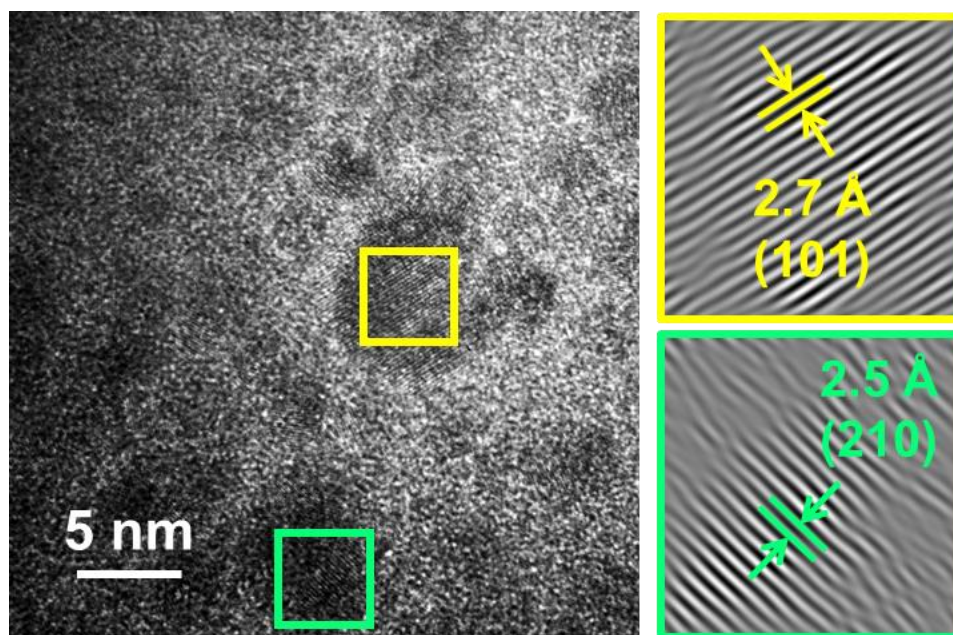


Figure S12. TEM images of C- β -Si₃N₄/50%Si sample after 300 charge–discharge cycles.

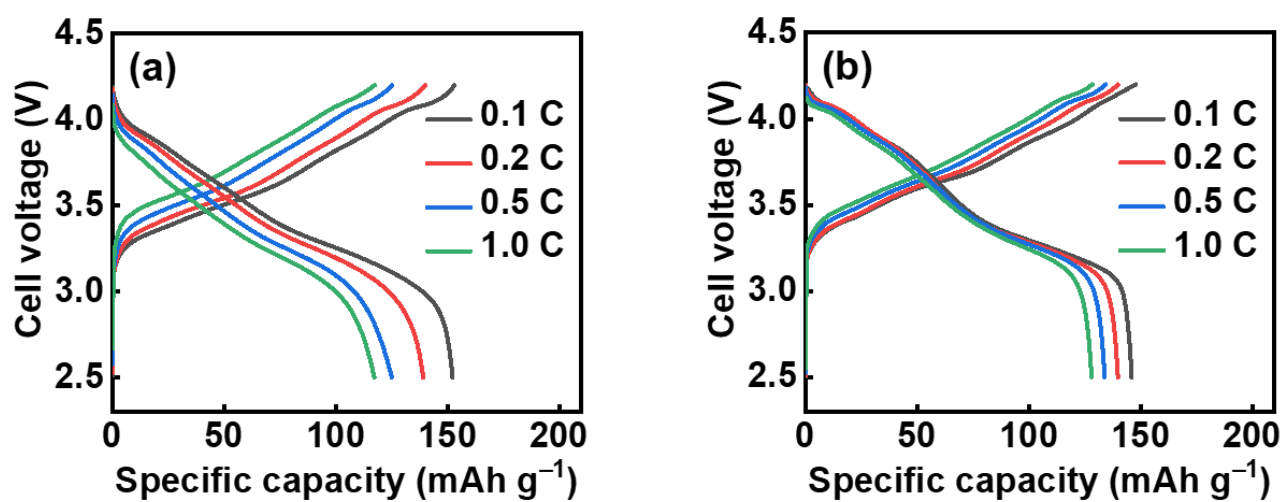


Figure S13. Charge–discharge curves of (a) C-β-Si₃N₄/50%Si||NMC-811 and (b) C-β-Si₃N₄/50%Si@AG||NMC-811 full cell measured at various rates. The specific capacities are calculated based on total mass of anode and cathode active materials.